



A Volume-of-Fluid-based numerical method for multi-component mass transfer with local volume changes



Stefan Fleckenstein, Dieter Bothe*

Technische Universität Darmstadt, Center of Smart Interfaces, Alarich-Weiss-Straße 10, 64287 Darmstadt, Germany

ARTICLE INFO

Article history:

Received 17 November 2014

Received in revised form 22 July 2015

Accepted 5 August 2015

Available online 14 August 2015

Keywords:

Mass transfer

Multi-component fluid

Local volume effects

DNS

Two-phase flow

ABSTRACT

This paper addresses the direct numerical simulation of conjugate multi-component mass transfer, taking into account the accompanying local volume effect. A rigorous derivation of a one-field formulation of the incompressible Navier–Stokes equations including volume effects is presented. A Volume-of-Fluid-based numerical method for the simulation of the resulting system of equations is developed and validated by comparison to analytical solutions in 1D and a semi-analytical test case in 3D. The implemented approach is applied to simulate the shrinking of a Taylor bubble with a pure gas phase in a square mini-channel and to the competing mass transfer in a multi-component mixture. The method can be used to study the local Sherwood numbers at fluid interfaces towards improving existing correlations for the prediction of mass transfer from rising bubbles.

© 2015 Elsevier Inc. All rights reserved.

1. Introduction

Optimal design, process control and efficient use of resources in multi-phase reactors for gas/liquid processes hinges on a precise understanding of the relevant processes which influence mass transfer. In common reactor types, such as bubble column reactors, these include deformation of the interface, chemical reactions, the presence of surface active substances, and the coupling between mass transfer and hydrodynamics, among others. Explicit analytical solutions to such highly complex coupled problems are not possible and simplified solutions or approximations are confined to their specific contexts, i.e. cannot be directly transferred to new situations. Numerical methods, on the other hand, do – in principle – not bear such limitations.

Direct Numerical Simulation (DNS), i.e. numerical solutions without model simplifications and under resolution of all relevant time and length scale, can be used to investigate the local processes of mass transfer at fluid interfaces and, hence, help to improve existing reactor designs and develop novel ones. This, however, requires to account for all relevant physical effects and transport phenomena which are present. While progress has been made on the simulation of mass transfer of dilute species, multi-component mass transfer and the implied volume effect has not yet been satisfactorily treated. Due to this reason, volume effects have mainly been studied by experimental means in the past, where the volume effect of mass transfer can never be entirely excluded. This is of particular importance for the dissolution of gas bubbles in a liquid has been specifically studied in experiments by, e.g., Takemura and Yabe [36] and Tomiyama et al. [38]. In the latter reference, a simplified model for the terminal volume of a dissolving CO₂ bubble in water is presented. Dissolution of gas bubbles has also been studied in contaminated systems with experimental methods [34,35,38].

* Corresponding author.

E-mail address: bothe@csi.tu-darmstadt.de (D. Bothe).

Since the present paper focuses on the treatment of local volume effects accompanying mass transfer, no general overview of the literature on the simulation of dilute species transfer is given here. For such an overview, the reader is referred to Bothe and Fleckenstein [4] and the exhaustive list of references given there. Also, the numerical method for (dilute) mass transfer which underlies the current work is explained in detail in [4].

While several authors have tried to incorporate volume effects into their numerical descriptions of (multi-component) mass transfer, these attempts have been confined to simplified geometries and flow types; see, e.g., Pigeonneau [22], Pigeonneau et al. [23], and Juncu [14]. Moreover, in these references, volume effects have not been considered as a local phenomenon, but only the total mass transfer at the interface has been used to compute a global shrinking rate of a bubble of fixed shape.

Hayashi and Tomiyama [12] developed a method for 2D simulations of local mass transfer at a deformable interface which takes into account the resulting volume effect. This method is then used to simulate the dissolution of a carbon dioxide bubble. However, the effect of mass transfer on the momentum balance is crucial since a change in volume is accompanied by a non-zero divergence of the velocity at the interface. But this effect of mass transfer on the flow is not taken into account there.

In contrast to multi-component mass transfer, numerical simulation of evaporation (i.e., thermally driven mass transfer) with local volume effects is an intensively studied subject and several numerical methods have been developed for systems composed of a single fluid. For instance, Juric and Tryggvason [15] presented a Front Tracking approach for the 2D simulation of phase change. Validation of the method is done by a 1D test case and the method is used to simulate film boiling. This phenomenon has also been studied based on the Volume-of-Fluid method by Welch and Wilson [40]. In the method developed there, a PLIC-based approach has been employed for transport of the volume fraction and the latter is recalculated in each interface cell after mass is transferred, in every time step, to align with the phase densities in a given cell.

A Volume-of-Fluid method has also been used by Hardt and Wondra [11], where the evaporation rate is smeared over a layer of cells around the interface. But note that the interface itself is kept sharp here by employing a PLIC approximation to the interface, and the numerical method is used to simulate film boiling. This method has been further applied to nucleate boiling by Kunkelmann and Stephan [17], where the numerical algorithm has been combined with a subgrid-scale model for the film thickness near the (underresolved) contact line. Contrary to the former approach, in the latter paper, a PLIC method is not used and the interface is distributed over several cells.

A 3D volume tracking approach for simulation of evaporation has been developed by Sato and Ničeno [29], who presented a numerical method for phase change due to evaporation. The method employs a color function to determine the position of the interface, which is located in cells intersecting the iso-surface with a value of 0.5 of the (interpolated) color function. Volume change and mass transfer are only computed for such interface cells. The method is validated by 1D and 3D test cases and nucleate boiling simulations with this method are compared to experiments.

A Volume-of-Fluid based method for the simulation of phase change has been developed in [31], where an iterative method is employed to satisfy the divergence condition for the velocity field in interface cells, resulting from the local volume change. This method accounts for the additional convective mass transfer (Stefan flow), if volume change is present. For validation, simulation results are compared to an analytic solution of a 1D test case and 3D simulations are compared to experimental measurements.

Ma and Bothe [18] derived a one-field formulation of the two-phase Navier–Stokes equation with thermally driven phase change by a volume averaging technique. This leads to a source term in the pressure correction of the velocity field, yielding the correct divergence condition in interface cells. A qualitative validation of the method has been performed with experimental results. This method is the basis for the numerical approach for multi-component mass transfer introduced in the present work.

2. Modeling

2.1. Continuum mechanical modeling of multi-component mass transfer

This section treats the basic continuum mechanical modeling of momentum and mass transfer in multi-phase flow which underlies the numerical method. The basic notation and principal set-up is given in Fig. 1. The domain Ω is decomposed into two disjoint subsets $\Omega^c(t)$, the *continuous phase*, and $\Omega^d(t)$, the *disperse phase*. The sets $\Omega^c(t)$ and $\Omega^d(t)$, also called the *bulk phase*, are separated by the two-dimensional surface $\Sigma(t)$, where we employ a sharp interface model. For better readability, the time dependence of the phases and the interface will be suppressed in the following. If a specific orientation of the interface normal \mathbf{n}_Σ is needed, we let it point into the disperse phase, as depicted in Fig. 1.

Since multi-component mass transfer is studied, each phase is considered to be a mixture of n species with a local mass density $\rho_k = \rho_k(t, \mathbf{x})$ for species k . Then, in absence of chemical reactions, conservation of mass for each chemical component k is described by the partial mass balance

$$\partial_t \rho_k + \operatorname{div}(\rho_k \mathbf{v}_k) = 0 \quad \text{in } \Omega \setminus \Sigma. \quad (1)$$

Here, \mathbf{v}_k is the individual velocity of component k , which, in a general setting, would be obtained as the solution of a partial momentum balance for species k . Taking the definition of the total density $\rho = \sum_k \rho_k$ and the total momentum

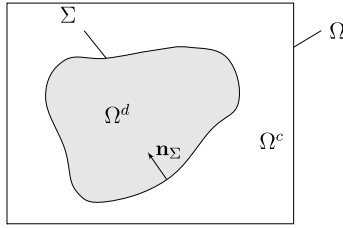


Fig. 1. Sketch of a generic domain and employed notation.

$\rho \mathbf{v} = \sum_k \rho_k \mathbf{v}_k$ of the mixture, the individual velocity can be expressed in terms of the barycentric velocity \mathbf{v} and the *diffusion velocity* \mathbf{u}_k defined as $\mathbf{u}_k = \mathbf{v}_k - \mathbf{v}$. Using this definition, Equation (1) becomes

$$\partial_t \rho_k + \operatorname{div}(\rho_k \mathbf{v} + \rho_k \mathbf{u}_k) = 0 \quad \text{in } \Omega \setminus \Sigma. \quad (2)$$

Employing the definition of the total momentum, the continuity equation

$$\partial_t \rho + \operatorname{div}(\rho \mathbf{v}) = 0 \quad \text{in } \Omega \setminus \Sigma \quad (3)$$

follows from the partial mass balances by summing over all constituents.

In order to obtain a closed system, additional jump conditions are needed for each individual component. Defining the *jump* $[[\phi]]$ of a quantity ϕ at Σ as

$$[[\phi]](x) = \lim_{h \rightarrow 0^+} (\phi(x + h \mathbf{n}_\Sigma) - \phi(x - h \mathbf{n}_\Sigma)), \quad x \in \Sigma, \quad (4)$$

we get

$$[[\rho_k(\mathbf{v}_k - \mathbf{v}^\Sigma)]] \cdot \mathbf{n}_\Sigma = 0 \quad \text{at } \Sigma \quad (5)$$

for component k , where the terms inside the jump bracket will be abbreviated as

$$\dot{m}_k := \rho_k^d(\mathbf{v}_k^d - \mathbf{v}^\Sigma) \cdot \mathbf{n}_\Sigma = \rho_k^c(\mathbf{v}_k^c - \mathbf{v}^\Sigma) \cdot \mathbf{n}_\Sigma, \quad (6)$$

the partial mass flux of species k across Σ . Note that \dot{m}_k is only defined at Σ . Again by summation over all constituents, we obtain the mass jump condition

$$[[\rho(\mathbf{v} - \mathbf{v}^\Sigma)]] \cdot \mathbf{n}_\Sigma = 0 \quad \text{at } \Sigma(t) \quad (7)$$

for the total mixture.

Using the molar mass M_k of a component k , we can recast the partial mass balance (2) in terms of the molar species concentration $c_k = \rho_k/M_k$, which yields

$$\partial_t c_k + \operatorname{div}(c_k \mathbf{v} + \mathbf{j}_k) = 0 \quad \text{in } \Omega \setminus \Sigma. \quad (8)$$

In this equation, the diffusive flux of species k , defined as $\mathbf{j}_k = c_k(\mathbf{v}_k - \mathbf{v})$, has been introduced. Then, the jump condition for molar mass reads

$$[[c_k(\mathbf{v}_k - \mathbf{v}^\Sigma)]] \cdot \mathbf{n}_\Sigma = 0 \quad \text{at } \Sigma(t) \quad (9)$$

for all $k = 1, \dots, n$. This can be rewritten as

$$[[c_k(\mathbf{v} - \mathbf{v}^\Sigma)]] \cdot \mathbf{n}_\Sigma + [[\mathbf{j}_k]] \cdot \mathbf{n}_\Sigma = 0 \quad \text{at } \Sigma(t), \quad (10)$$

where the definition of the diffusive flux \mathbf{j}_k has been used. With this representation of the jump condition it becomes obvious that mass transfer at an interface always leads to a movement of Σ relative to the phases, i.e., is accompanied by local volume effects.

The interfacial mass balance (10) needs to be complemented by a constitutive relation between the one-sided limits of the bulk concentrations at Σ . Here we employ Henry's law which, in the form for molar concentrations, states that

$$c_k^c = c_k^d/H_k \quad \text{at } \Sigma(t) \quad (11)$$

with a model parameter H_k (the so-called Henry coefficient) which we consider constant here for simplicity; for more details cf. Bothe and Fleckenstein [4] and the references given there.

The diffusive fluxes need to be modeled via material dependent constitutive equations. In the general case of multi-component diffusion in non-dilute solutions, this requires a rather involved modeling using the Maxwell–Stefan equations with generalized thermodynamic driving forces. For more details on this approach, the reader is referred to Taylor and

Krishna [37] and to Bothe and Dreyer [3] for a rigorous derivation within continuum-thermodynamics. However, in the cases being simulated here, both phases are composed of a dilute mixture, although with different major components. Note that this involves the transfer of components being non-dilute in one and dilute in the other phase. In this situation, the molecular transport of the dilute components can well be modeled by Fickian diffusion, i.e., as $\mathbf{j}_k = -D_k \nabla c_k$.

Furthermore, we can then consider each phase as an incompressible Newtonian fluid. This incompressibility assumption in the gas phase is justified since in the applications we have in mind, the relevant velocities are small compared to the speed of sound. The bulk momentum balances are hence given by the Navier–Stokes equations,

$$\partial_t(\rho \mathbf{v}) + \operatorname{div}(\rho \mathbf{v} \otimes \mathbf{v}) - \operatorname{div} \mathbf{T} = \rho \mathbf{g} \quad \text{in } \Omega \setminus \Sigma, \quad (12)$$

$$\operatorname{div} \mathbf{v} = 0 \quad \text{in } \Omega \setminus \Sigma. \quad (13)$$

For the considered Newtonian fluids, the stress tensor is given by

$$\mathbf{T} = -p\mathbf{I} + \mathbf{S} \quad (14)$$

with the viscous stress tensor $\mathbf{S} = \eta(\nabla \mathbf{v} + \nabla \mathbf{v}^T)$ for incompressible fluids, where η is the dynamic viscosity which is assumed constant inside the individual fluid phases. The pressure is defined as $p = -\frac{1}{3} \operatorname{tr}(\mathbf{T})$.

The interfacial momentum transmission condition is given by Slattery et al. [33]

$$\llbracket \rho \mathbf{v} \otimes (\mathbf{v} - \mathbf{v}^\Sigma) + p\mathbf{I} - \mathbf{S} \rrbracket \cdot \mathbf{n}_\Sigma = \sigma \kappa \mathbf{n}_\Sigma + \nabla_\Sigma \sigma \quad \text{on } \Sigma. \quad (15)$$

Here, it is assumed that Σ does not carry mass and has no intrinsic (surface) viscosities. Furthermore, $\kappa = \operatorname{div}_\Sigma(-\mathbf{n}_\Sigma)$ denotes the local curvature (twice the mean curvature) of the interface in which $\operatorname{div}_\Sigma$ is the surface divergence. For simplicity, we will assume the surface tension σ to be constant. Since only viscous fluids are considered here, we assume that the tangential component of the interfacial velocity jump vanishes, i.e.

$$\mathbf{P}_\Sigma \llbracket \mathbf{v} \rrbracket = 0, \quad (16)$$

where $\mathbf{P}_\Sigma := \mathbf{I} - \mathbf{n}_\Sigma \otimes \mathbf{n}_\Sigma$ is the projection onto the local tangent plane. Moreover, the tangential component of the interface velocity \mathbf{v}^Σ is assumed to coincide with the one-sided limits of the tangential part of the bulk velocities, i.e.,

$$\mathbf{v}^d_\parallel = \mathbf{v}^c_\parallel = \mathbf{v}^\Sigma_\parallel. \quad (17)$$

Now, if no mass transfer occurs, the velocity at the interface coincides with the interface velocity \mathbf{v}^Σ and the first term on the left-hand side of (15) vanishes. In the general case, employing (7), the first term in (15) becomes

$$\llbracket \rho \mathbf{v} \otimes (\mathbf{v} - \mathbf{v}^\Sigma) \cdot \mathbf{n}_\Sigma \rrbracket = \dot{m} \llbracket \mathbf{v} \rrbracket = \dot{m}^2 \left\llbracket \frac{1}{\rho} \right\rrbracket \mathbf{n}_\Sigma, \quad (18)$$

where $\dot{m} = \rho(\mathbf{v} - \mathbf{v}^\Sigma) \cdot \mathbf{n}_\Sigma$ is the mass flux across Σ . Hence, the interfacial momentum jump condition becomes

$$\llbracket p\mathbf{I} - \mathbf{S} \rrbracket \cdot \mathbf{n}_\Sigma = \sigma \kappa \mathbf{n}_\Sigma - \dot{m}^2 \left\llbracket \frac{1}{\rho} \right\rrbracket \mathbf{n}_\Sigma \quad \text{at } \Sigma. \quad (19)$$

Considering typical values of the involved parameters for mass transfer from a gas bubble in water with a radius of $r = 1$ mm and with the assumption that the bubble needs at least one second to dissolve completely, we can estimate the relative size of the terms on the right-hand side of (19). The relative velocity of the phases is given by the shrinking velocity, estimated as $(\mathbf{v} - \mathbf{v}^\Sigma) \cdot \mathbf{n}_\Sigma \approx 10^{-3}$ m/s. This yields

$$\dot{m}^2 \left\llbracket \frac{1}{\rho} \right\rrbracket \approx (\rho^{\text{air}}(\mathbf{v} - \mathbf{v}^\Sigma) \cdot \mathbf{n}_\Sigma)^2 \frac{1}{\rho^{\text{air}}} \approx 10^{-6} \text{ N/m}^2. \quad (20)$$

Moreover, estimating the surface force yields

$$\sigma \kappa \approx 72 \times 10^{-3} \text{ N m}^{-1} \cdot 1/10^{-3} \text{ m}^{-1} \approx 10^2 \text{ N/m}^2. \quad (21)$$

Since the surface tension is several orders of magnitude larger than the contribution of the phase change, the simplified jump conditions

$$\mathbf{P}_\Sigma \llbracket \mathbf{v} \rrbracket = 0 \quad \text{at } \Sigma, \quad (22)$$

$$\llbracket p\mathbf{I} - \mathbf{S} \rrbracket \cdot \mathbf{n}_\Sigma = \sigma \kappa \mathbf{n}_\Sigma \quad \text{at } \Sigma \quad (23)$$

can often be employed. Note, however, that in other cases, like strong evaporation and formation or collapse of a cavitation bubble, this simplification may not be valid. In thermally driven mass transfer, the effect modeled by (20) is known as vapor recoil; see, e.g., the modeling in [18].

2.2. Derivation of a one-field formulation for mass transfer with volume change

Mass transfer is always accompanied by volume effects. Although not significant in some applications, volume change is of utmost importance in particular for the rise of bubbles of a pure gas in water or other solvents. Such bubbles can dissolve within a few seconds in case of high solubility of the gas in water; cf. Takemura and Yabe [34]. In the following sections, equations are derived which incorporate the volume effect due to mass transfer in a fluid mixture consisting of several individual components. The derivation of these equations is performed using averaging techniques as can be found in [32] or [13]. This intermediate step between the classical continuum equations and the implementation into a VOF-code is done to obtain a one-field formulation of the momentum and mass balance which is suitable for a numerical method.

For the reader's convenience, the employed averaging tools are collected in Appendix A. The averaging process mitigates the problem of discontinuous or singular quantities which appear in multi-phase flows in the form of surface tension, Marangoni stresses, pressure and density jumps among others and which must be treated with specific methods in order to obtain an accurate numerical method. Averaging techniques as presented below have, e.g., already been applied to derive a one-field formulation of the two-phase Navier–Stokes equations in case of evaporation of a pure liquid phase in an inert ambient gas by Ma and Bothe [18]. For more details on the derivation of such models, see, e.g., [41].

Before going into the detailed derivations, let us stress the fact that diverse averages especially of the velocities are in use which have to be carefully distinguished in order to avoid inconsistent models. This is the main reason why we have chosen to give the derivations in rather full detail.

2.2.1. Transport of the volume fraction

In this section, a transport equation for the volume fraction $f^k = \langle \chi^k \rangle_V$ is derived, i.e., for the relative amount of phase Ω^k in the control volume V . A derivation of this equation based on averaging has already been given in [19], but is included here for completeness. For brevity of notation, we will drop the spatial variable in the following and use V instead of $V(\mathbf{x}) = \mathbf{x} + V_0$, where V_0 is a fixed volume.

In order to derive equations which are suitable for numerical computations, the following averaging operators are employed, see [32] or [13] for more details. The *volume average* over the phase Ω^k of the quantity ϕ existing in the bulk $\Omega \setminus \Sigma$ is defined as

$$\langle \phi \rangle_{V^k}^V = \frac{1}{|V|} \int_{V^k} \phi dV \quad (24)$$

and the *phase average* over phase Ω^k of ϕ is analogously defined as

$$\langle \phi \rangle_{V^k} = \langle \phi \rangle_{V^k}^{V^k} = \frac{1}{|V^k|} \int_{V^k} \phi dV. \quad (25)$$

Taking the volume average, the volume fraction of phase Ω^k in the control volume V is defined as

$$f^k = \langle 1 \rangle_{V^k}^V = \frac{1}{|V|} \int_{V^k} 1 dV = \frac{1}{|V|} \int_V \chi_{\Omega^k} dV = \frac{|V^k|}{|V|}. \quad (26)$$

The two averaging procedures above are related by

$$\langle \phi \rangle_{V^k}^V = \frac{|V^k|}{|V|} \frac{1}{|V^k|} \int_{V^k} \phi dV = f^k \langle \phi \rangle_{V^k}. \quad (27)$$

Similarly, for a quantity defined at the interface, the average $\langle \phi \rangle_\Sigma^V$ is understood in the sense

$$\langle \phi \rangle_{\Sigma_V}^V = \frac{1}{|V|} \int_{\Sigma_V} \phi dA, \quad (28)$$

where $\Sigma_V := \Sigma \cap V$. For simplicity of notation, we also write $\langle \phi \rangle_\Sigma^V$.

With the definitions given above, we can derive a balance for the volume fraction. Starting from the local mass balance (3), volume averaging over phase Ω^k yields

$$\langle \partial_t \rho \rangle_{V^k}^V + \langle \text{div}(\rho \mathbf{v}) \rangle_{V^k}^V = 0 \quad \text{in } \Omega. \quad (29)$$

Then, applying (A.1) and (A.3), we obtain

$$\partial_t \langle \rho \rangle_{V^k}^V + \text{div} \langle \rho \mathbf{v} \rangle_{V^k}^V = - \langle \rho (\mathbf{v} - \mathbf{v}^\Sigma) \cdot \mathbf{n}^k \rangle_\Sigma^V = - \langle \dot{m} \rangle_\Sigma^V \mathbf{n}^k \cdot \mathbf{n}_\Sigma \quad \text{in } \Omega, \quad (30)$$

with \mathbf{n}^k denoting the outer normal of Ω^k ; note that $\mathbf{n}^k \cdot \mathbf{n}_\Sigma \equiv \pm 1$. Exploiting constant density ρ^k inside the control volume V in the specific bulk phase, we get

$$\rho^k (\partial_t f^k + \operatorname{div}(f^k \langle \mathbf{v} \rangle_{V^k})) = -\langle \dot{m} \rangle_\Sigma^V \mathbf{n}^k \cdot \mathbf{n}_\Sigma \quad \text{in } \Omega. \quad (31)$$

Employing $\operatorname{div}(\langle \mathbf{v} \rangle_{V^k}) \approx \langle \operatorname{div} \mathbf{v} \rangle_{V^k}$ by (A.10) and $\operatorname{div} \mathbf{v} = 0$, we obtain

$$\partial_t f^k + \langle \mathbf{v} \rangle_{V^k} \cdot \nabla f^k = -\frac{\langle \dot{m} \rangle_\Sigma^V}{\rho^k} \mathbf{n}^k \cdot \mathbf{n}_\Sigma \quad \text{in } \Omega \quad (32)$$

as an accurate approximation for sufficiently small control volumes; the latter is necessarily valid in the Direct Numerical Simulations, since full resolution of the hydrodynamics is essential to capture the much smaller scales of the species distribution.

In the following, the notation $f = f^d$ will be used for the disperse phase volume fraction and referred to as *the* volume fraction.

2.2.2. Derivation of the two-scalar method for chemical species

For an individual constituent of the fluid mixture, the transport equation in phase Ω^k is derived from the local balance equation (8). Similar to the procedure in Section 2.2.1 we get

$$\partial_t \langle c_i \rangle_{V^k}^V + \operatorname{div} \langle c_i \mathbf{v} \rangle_{V^k}^V + \operatorname{div} \langle \mathbf{j}_i \rangle_{V^k}^V = -\frac{1}{M_i} \langle \dot{m}_i \rangle_\Sigma^V \mathbf{n}^k \cdot \mathbf{n}_\Sigma \quad \text{in } \Omega. \quad (33)$$

The dominant length scale of the species transport is the scale of the concentration field, which is smaller than the scales of the velocity field by a factor of $\sqrt{Sc_i}$, where Sc_i denotes the Schmidt number for species i . Since the primary interest in this paper is mass transfer, the concentration gradients must be fully resolved in a numerical simulation. Therefore, we will assume for the modeling that the velocity field is approximately constant on the length scale of a grid cell. Then, the convective term in Equation (33) can be approximated by

$$\operatorname{div} \langle c_i \mathbf{v} \rangle_{V^k}^V \approx \operatorname{div}(\langle c_i \rangle_{V^k}^V \langle \mathbf{v} \rangle_{V^k}^V) = \operatorname{div}(\langle c_i \rangle_{V^k}^V \langle \mathbf{v} \rangle_{V^k}^V). \quad (34)$$

Note that this imposes a condition on the grid resolution to be employed in the numerical method. Hence, with $\phi_i^k := \langle c_i \rangle_{V^k}^V$ and using (A.10) together with $\operatorname{div} \mathbf{v} = 0$, the two-scalar balance equation

$$\partial_t \phi_i^k + \langle \mathbf{v} \rangle_{V^k} \cdot \nabla \phi_i^k + \operatorname{div} \langle \mathbf{j}_i \rangle_{V^k}^V = -\frac{\mathbf{n}^k \cdot \mathbf{n}_\Sigma}{M_i} \langle \dot{m}_i \rangle_\Sigma^V \quad \text{in } \Omega \quad (35)$$

results. The numerical implementation of this transport equation has to be deferred until Section 4 below, since some further modeling issues need to be introduced first.

With the individual mass fluxes determined according to Equation (35), the change of volume due to mass transfer can be computed, since the total mass flux \dot{m} is the sum of all partial mass fluxes \dot{m}_i over the interface. However, as already noted in Section 2.1, the mass flux \dot{m}_i of an individual component contains both a diffusive and a convective part,

$$\dot{m}_i = \rho_i (\mathbf{v}_i - \mathbf{v}^\Sigma) \cdot \mathbf{n}_\Sigma = \rho_i (\mathbf{v} - \mathbf{v}^\Sigma) \cdot \mathbf{n}_\Sigma + \mathbf{J}_i \cdot \mathbf{n}_\Sigma \quad (36)$$

with $\mathbf{J}_i = \rho_i \mathbf{u}_i = M_i \mathbf{j}_i$. As explained above, we consider dilute mixtures in both phases for which the diffusive fluxes are modeled by Fickian diffusion, i.e.,

$$\mathbf{J}_i = -M_i D_i \nabla c_i = -D_i \nabla \rho_i. \quad (37)$$

Under the given assumption of dilute components in the liquid phase and if the main component of the liquid is only weakly soluble in the gas phase, the mass flux across the interface of a single component can be computed from the relations

$$\dot{m}_i = y_i \dot{m} + \mathbf{J}_i \cdot \mathbf{n}_\Sigma = y_i \sum_{l=1}^{n-1} \dot{m}_l + \mathbf{J}_i \cdot \mathbf{n}_\Sigma, \quad (38)$$

for all $i = 1, \dots, n-1$, where species n is the solvent which is considered to be insoluble in the gas phase. This leads to the $(n-1) \times (n-1)$ -system

$$\begin{pmatrix} 1-y_1 & -y_1 & \dots & & \\ -y_2 & 1-y_2 & \ddots & & \\ & \ddots & \ddots & \ddots & \\ \vdots & & & -y_{n-2} & \\ & & & -y_{n-1} & 1-y_{n-1} \end{pmatrix} \begin{pmatrix} \dot{m}_1 \\ \vdots \\ \dot{m}_{n-1} \end{pmatrix} = \begin{pmatrix} \mathbf{J}_1 \cdot \mathbf{n}_\Sigma \\ \vdots \\ \mathbf{J}_{n-1} \cdot \mathbf{n}_\Sigma \end{pmatrix}. \quad (39)$$

The matrix on the left-hand side is of the form $\mathbf{I} - \mathbf{y} \otimes \mathbf{1}$ with the vector $\mathbf{y} = (y_1, \dots, y_{n-1})^\top$ and $\mathbf{1} = (1, \dots, 1)^\top$. It has the inverse

$$(\mathbf{I} - \mathbf{y} \otimes \mathbf{1})^{-1} = \mathbf{I} + \frac{\mathbf{y} \otimes \mathbf{1}}{1 - \sum_{i=1}^{n-1} y_i}, \quad (40)$$

by which the mass flux of species i can be computed. For a single dilute transfer component, as for instance in standard evaporation, this yields a total mass flux of

$$\dot{m} = -\frac{\rho D_1}{1 - y_1} \nabla y_1 \cdot \mathbf{n}_\Sigma, \quad (41)$$

in accordance with the formula used in [31].

2.2.3. A one-field formulation for momentum transport with volume change due to mass transfer

In this section, a one-field formulation of the two-phase Navier–Stokes equations with volume change is derived. Starting point are the volume averaged Navier–Stokes equations

$$\langle \partial_t(\rho \mathbf{v}) \rangle_{V_k}^V + \langle \text{div}(\rho \mathbf{v} \otimes \mathbf{v}) \rangle_{V_k}^V = \langle -\nabla p + \text{div} \mathbf{S} \rangle_{V_k}^V + \langle \rho \mathbf{g} \rangle_{V_k}^V. \quad (42)$$

Applying the averaging rules (A.1) and (A.3), this becomes

$$\begin{aligned} \partial_t \langle \rho \mathbf{v} \rangle_{V_k}^V + \text{div} \langle \rho \mathbf{v} \otimes \mathbf{v} \rangle_{V_k}^V \\ = -\nabla \langle p \rangle_{V_k}^V + \text{div} \langle \mathbf{S} \rangle_{V_k}^V + \langle \rho \rangle_{V_k}^V \mathbf{g} - \langle \rho^k \mathbf{v}^k (\mathbf{v}^k - \mathbf{v}^\Sigma) \cdot \mathbf{n}^k - \mathbf{T}^k \cdot \mathbf{n}^k \rangle_{V_k}^V, \end{aligned} \quad (43)$$

where $\mathbf{T}^k = -p^k \mathbf{I} + \mathbf{S}^k$. We again assume constant density ρ^k inside the bulk phase Ω^k and sum over the phases $k = c, d$. Considering each term separately, we obtain the following contributions:

$$\partial_t \left(\langle \rho \mathbf{v} \rangle_{V_d}^V + \langle \rho \mathbf{v} \rangle_{V_c}^V \right) = \partial_t (\rho_V \mathbf{v}_m), \quad (44)$$

where $\rho_V := \langle \rho \rangle_V = f^d \rho^d + f^c \rho^c$ is the volume averaged density and \mathbf{v}_m is the *barycentric averaged velocity* given as

$$\mathbf{v}_m := \frac{f \rho^d \langle \mathbf{v} \rangle_{V_d}^V + (1 - f) \rho^c \langle \mathbf{v} \rangle_{V_c}^V}{f \rho^d + (1 - f) \rho^c}. \quad (45)$$

The convective term becomes

$$\sum_{k=c,d} \langle \rho \mathbf{v} \otimes \mathbf{v} \rangle_{V_k}^V = \rho_V \mathbf{v}_m \otimes \mathbf{v}_m + \frac{f^d f^c \rho^d \rho^c}{f^d \rho^d + f^c \rho^c} \mathbf{v}_r \otimes \mathbf{v}_r, \quad (46)$$

with $\mathbf{v}_r = \langle \mathbf{v} \rangle_{V_d}^V - \langle \mathbf{v} \rangle_{V_c}^V$ denoting the relative velocity of the phases. This relation is only approximate and will be further discussed below, up to (58).

For the pressure, we get

$$\sum_{k=c,d} \langle p \rangle_{V_k}^V = f^d \langle p \rangle_{V_d}^V + f^c \langle p \rangle_{V_c}^V =: p_V. \quad (47)$$

The final contribution is the averaged viscous stress, i.e.,

$$\begin{aligned} \sum_{k=c,d} \langle \mathbf{S} \rangle_{V_k}^V &= (\nabla(\eta_V \mathbf{v}_m) + \nabla(\eta_V \mathbf{v}_m)^T) + \nabla \left(\mathbf{v}_r \frac{f^c f^d}{\rho_V} (\rho^c \eta^d - \rho^d \eta^c) \right) + \nabla \left(\mathbf{v}_r \frac{f^c f^d}{\rho_V} (\rho^c \eta^d - \rho^d \eta^c) \right)^T \\ &\quad + \sum_{k=c,d} \eta^k \left(\langle \mathbf{v}^k \otimes \mathbf{n}^k \rangle_\Sigma^V + \langle \mathbf{n}^k \otimes \mathbf{v}^k \rangle_\Sigma^V \right). \end{aligned} \quad (48)$$

Here, the average viscosity η_V is defined as $\eta_V = f^d \eta^d + f^c \eta^c$, in an analogous manner as the volume averaged density ρ_V .

For mass transfer from bubbles it will be shown below that $|\mathbf{v}_r| \ll |\mathbf{v}_m|$ for volume change due to chemically driven mass transfer and we will thus disregard the terms containing \mathbf{v}_r in the following. This yields

$$\partial_t (\rho_V \mathbf{v}_m) + \text{div} (\rho_V \mathbf{v}_m \otimes \mathbf{v}_m) = \text{div} (\nabla(\eta_V \mathbf{v}_m) + \nabla(\eta_V \mathbf{v}_m)^T) - \nabla p_V + \rho_V \mathbf{g} + \mathbf{f}^\Sigma$$

as the one-field formulation of the Navier–Stokes equations, where

$$\mathbf{f}^\Sigma := \langle \llbracket \rho \mathbf{v} (\mathbf{v} - \mathbf{v}^\Sigma) \cdot \mathbf{n}_\Sigma - \mathbf{T} \cdot \mathbf{n}_\Sigma \rrbracket \rangle_\Sigma^V. \quad (49)$$

Inserting the interfacial momentum jump condition yields $\mathbf{f}^\Sigma = \langle \sigma \kappa \mathbf{n}_\Sigma \rangle_\Sigma^V$ in the considered case of constant surface tension.

The relative velocity of the phases

The (averaged) relative velocity of the phases at the interface in normal direction can be computed as

$$\mathbf{v}_r^n := \frac{1}{|\Sigma|} \int_{\Sigma} \llbracket \mathbf{v} \rrbracket \cdot \mathbf{n}_{\Sigma} dA = \frac{1}{|\Sigma|} \int_{\Sigma} \dot{m} \left\llbracket \frac{1}{\rho} \right\rrbracket dA = \langle \dot{m} \rangle_{\Sigma} \left\llbracket \frac{1}{\rho} \right\rrbracket, \quad (50)$$

assuming constant density of the phases at least in a neighborhood of Σ . Then, by using the one-sided limits \mathbf{v}^d and \mathbf{v}^c of the disperse phase and continuous phase velocities, the left-hand side in the last equation reads

$$\frac{1}{|\Sigma|} \int_{\Sigma} \llbracket \mathbf{v} \rrbracket \cdot \mathbf{n}_{\Sigma} dA = \frac{1}{|\Sigma|} \int_{\Sigma} (\mathbf{v}^d - \mathbf{v}^c) \cdot \mathbf{n}_{\Sigma} dA \quad (51)$$

$$\approx \left(\frac{1}{|\Sigma|} \int_{\Sigma} \mathbf{v}^d dA - \frac{1}{|\Sigma|} \int_{\Sigma} \mathbf{v}^c dA \right) \cdot \langle \mathbf{n}_{\Sigma} \rangle_{\Sigma} = \mathbf{v}_r \cdot \langle \mathbf{n}_{\Sigma} \rangle_{\Sigma}. \quad (52)$$

In this calculation, it is assumed that the control volume is small enough so that the interface normal \mathbf{n}_{Σ} is well approximated by its average $\langle \mathbf{n}_{\Sigma} \rangle_{\Sigma}$. For small control volumes V , the one-sided limits of \mathbf{v}^k at Σ can be replaced by $\langle \mathbf{v}^k \rangle_{V^k}$, which leads to the relation

$$\mathbf{v}_r \cdot \langle \mathbf{n}_{\Sigma} \rangle_{\Sigma} = (\langle \mathbf{v} \rangle_{V^d} - \langle \mathbf{v} \rangle_{V^c}) \cdot \langle \mathbf{n}_{\Sigma} \rangle_{\Sigma} = \langle \dot{m} \rangle_{\Sigma} \left\llbracket \frac{1}{\rho} \right\rrbracket, \quad (53)$$

for the relative velocity in normal direction of the interface.

For finite-sized control volumes, a relative motion of the phase averaged velocities in tangential direction of the interface occurs in general. Since continuity of the (pointwise) tangential velocities in the continuum mechanical model was assumed, i.e. $\llbracket \mathbf{v} \rrbracket \cdot \boldsymbol{\tau} = 0$ for all $\boldsymbol{\tau}$ perpendicular to \mathbf{n}_{Σ} , the averaged tangential relative velocity in the control volume V can be estimated via

$$(\langle \mathbf{v} \rangle_{V^d} - \langle \mathbf{v} \rangle_{V^c})_{\parallel} = \langle \mathbf{v}_{\parallel} - \mathbf{v}^d(\mathbf{x}_0)_{\parallel} \rangle_{V^d} - \langle \mathbf{v}_{\parallel} - \mathbf{v}^c(\mathbf{x}_0)_{\parallel} \rangle_{V^c}. \quad (54)$$

Here, we used the fact that for $\mathbf{x}_0 \in \Sigma$, the equality $\mathbf{v}^d(\mathbf{x}_0)_{\parallel} = \mathbf{v}^c(\mathbf{x}_0)_{\parallel}$ is satisfied for the one-sided limits of the velocities at Σ . Then, for both terms on the right-hand side of (54), we have the estimate

$$\left| \frac{1}{|V^k|} \int_{V^k} (\mathbf{v}^k(\mathbf{x}) - \mathbf{v}^k(\mathbf{x}_0))_{\parallel} d\mathbf{x} \right| \leq \frac{1}{|V^k|} \int_{V^k} |\mathbf{v}^k(\mathbf{x}) - \mathbf{v}^k(\mathbf{x}_0)| d\mathbf{x} \quad (55)$$

$$\leq \frac{1}{|V^k|} \int_{V^k} \|\nabla \mathbf{v}^k\|_{\infty, V^k} |\mathbf{x} - \mathbf{x}_0| d\mathbf{x} \quad (56)$$

$$\leq C \text{diam}(V^k) \leq C \text{diam}(V). \quad (57)$$

Thus, for the purpose of numerical simulations, we assume that the tangential contribution to the relative velocity \mathbf{v}_r vanishes. Hence, we have the approximate relation

$$\mathbf{v}_r = \langle \mathbf{v} \rangle_{V^d} - \langle \mathbf{v} \rangle_{V^c} = \langle \dot{m} \rangle_{\Sigma} \left\llbracket \frac{1}{\rho} \right\rrbracket \langle \mathbf{n}_{\Sigma} \rangle_{\Sigma}, \quad (58)$$

which has already been employed by Ma and Bothe [18] without detailed justification. Note that, due to our previous assumption that the mass density within a phase in a given control volume is constant, we can replace $\left\llbracket \frac{1}{\rho} \right\rrbracket$ by $\left(\frac{1}{\rho^d} - \frac{1}{\rho^c} \right)$ in the last equation.

Defining the *volume averaged velocity*

$$\mathbf{v}_V := f \langle \mathbf{v} \rangle_{V^d} + (1 - f) \langle \mathbf{v} \rangle_{V^c}, \quad (59)$$

where V is the averaging volume, $V^k = V \cap \Omega^k$ and $\rho^k = \langle \rho \rangle_{V^k}$ denotes the average density inside V^k , the relative and the barycentric velocities are related by

$$\mathbf{v}_m = \mathbf{v}_V + \llbracket \rho \rrbracket \frac{f(1-f)}{\rho_V} \mathbf{v}_r. \quad (60)$$

Such a term containing the relative velocity of the phases has been derived earlier by Sabisch [28] for two-phase flow without volume effects and by Wörner et al. [42], where also an algebraic closure for the relative velocity has been proposed. There, this term is called drift-flux term and becomes particularly significant if the flow structure is poorly resolved [28].

In addition to (60), a relation between the divergence of \mathbf{v}_V and the relative velocity can be obtained. An expression for the divergence of the volume averaged velocity can be derived from Equation (32), respectively from the conservative form (31). Summing over $k = c, d$ yields

$$\partial_t 1 + \operatorname{div}(f \langle \mathbf{v} \rangle_{V^d} + (1-f) \langle \mathbf{v} \rangle_{V^c}) = \langle \dot{m} \rangle_\Sigma^V \left(\frac{1}{\rho^d} - \frac{1}{\rho^c} \right); \quad (61)$$

recall that we let the interface normal \mathbf{n}_Σ point into phase Ω^d . Hence, the divergence of the volume averaged velocity is

$$\operatorname{div} \mathbf{v}_V = \langle \dot{m} \rangle_\Sigma^V \left(\frac{1}{\rho^d} - \frac{1}{\rho^c} \right) = \langle \dot{m} \rangle_\Sigma^V \left\| \frac{1}{\rho} \right\|. \quad (62)$$

Analogously, summing over $k = c, d$ for the non-conservative form of Equation (32) gives

$$(\langle \mathbf{v} \rangle_{V^d} - \langle \mathbf{v} \rangle_{V^c}) \cdot \nabla f = \langle \dot{m} \rangle_\Sigma^V \left(\frac{1}{\rho^d} - \frac{1}{\rho^c} \right), \quad (63)$$

which yields

$$(\langle \mathbf{v} \rangle_{V^d} - \langle \mathbf{v} \rangle_{V^c}) \cdot \frac{\nabla f}{\|\nabla f\|} \|\nabla f\| = \langle \dot{m} \rangle_\Sigma^V \left\| \frac{1}{\rho} \right\|. \quad (64)$$

With (62) and the definition of the interface normal, we obtain

$$\mathbf{v}_r \cdot \mathbf{n}_\Sigma^{\text{num}} \|\nabla f\| = \operatorname{div} \mathbf{v}_V, \quad (65)$$

where $\mathbf{n}_\Sigma^{\text{num}}$ is the numerical approximation of the interface normal obtained from ∇f . If the interface is sufficiently resolved, as has to be done for a DNS, we may identify $\mathbf{n}_\Sigma^{\text{num}}$ with the true interface normal.

Now, performing an order-of-magnitude estimation of the terms on the right-hand side of Equation (60), we see that the last term in (60) gives only a minor contribution to the total momentum for a bubble rising in a liquid and shrinking due to mass transfer. To come to this conclusion, we estimate the relative velocity of the phases by employing (58), where the mass flux is calculated using a diffusion coefficient of $D = 10^{-9} \text{ m}^2/\text{s}$ with a typical thickness of the concentration boundary layer of $\delta = 10^{-6} \text{ m}$, a Henry coefficient of $H = 33$ corresponding to the dissolution of oxygen in water at standard conditions and densities $\rho^c = 10^3 \frac{\text{kg}}{\text{m}^3}$ and $\rho^d = 1 \frac{\text{kg}}{\text{m}^3}$. Then,

$$\mathbf{v}_r \approx D \frac{\rho_\Sigma - \rho(\delta)}{\delta} \approx D \frac{\rho^d/H}{\delta} \approx 10^{-5} \text{ m/s}. \quad (66)$$

Even for very good solubilities, e.g. of carbon dioxide in water with a Henry coefficient of $H \approx 1.2$ at standard conditions, the relative velocity is below $\mathbf{v}_r \approx 10^{-3} \text{ m/s}$. The prefactor of \mathbf{v}_r in the last term is estimated to be of order unity. The volume averaged velocity is estimated as being of the same order of magnitude as the rise velocity of the bubble, i.e. $\mathbf{v}_V \approx 0.2 \text{ m/s}$. Hence, the contribution of the relative velocity to the barycentric velocity is not significant and will be neglected. In the numerical scheme introduced below the divergence of the barycentric velocity is approximated according to

$$\operatorname{div} \mathbf{v}_m \approx \operatorname{div} \mathbf{v}_V. \quad (67)$$

Hence, the source term for the pressure Poisson equation is calculated as

$$\zeta = \operatorname{div} \mathbf{v}_V = \langle \dot{m} \rangle_\Sigma^V \left\| \frac{1}{\rho} \right\|. \quad (68)$$

Note that we effectively assume that the barycentric velocity and the volume averaged velocity coincide in the entire computational domain. However, since the difference of these two velocities may be significant in cases where the simplification above cannot be made, we continue to distinguish between these quantities below.

Taking the relative velocity $\mathbf{v}_r = 10^{-3} \text{ m/s}$ as above and the barycentric velocity as $\mathbf{v}_m = 0.2 \text{ m/s}$, where the last estimate is based on the typical rise velocity of a 1 mm bubble, we see that the relative velocity can be neglected in the one-field formulation of the Navier–Stokes equations.

3. VOF-based numerical method for mass transfer of dilute species

In this work, we employ the Volume-of-Fluid-based in-house code *FS3D*, originally being developed by Rieber [26]. *FS3D* has been validated for fluid dynamics simulations, including droplet impacts and collisions [26,9,8], bubble flow [16] and falling films [1]. A detailed account of the numerical method for hydrodynamics simulations can be found in [25].

Let us briefly review the Volume-of-Fluid (VOF) approach since it is tightly connected to our numerical approach to mass transfer, particularly if volume effects are considered. The VOF-method utilizes a Finite Volume scheme to transport the volume fraction f in a control volume V . In the numerical implementation of this method, the control volumes correspond

to grid cells. With $f = f^d$ as above being the volume fraction of Ω^d , the disperse phase is present in cells where $f > 0$ and the continuous phase is present in cells where $f < 1$. Moreover, the interface intersects all cells for which $0 < f < 1$.

To track the change of volume fraction inside a control volume, the transport equation

$$\partial_t f + \mathbf{v} \cdot \nabla f = 0 \quad (69)$$

is solved. For geometrically consistent initial distributions of f , the interface is located in a single layer of cells. In order to avoid smearing of the interface over several cell layers during advection of the f -field, a geometry-based flux calculation using the so-called piecewise linear interface calculation (PLIC) method [24] is employed. In this approach, the volume fraction distribution is reconstructed linearly in every interface cell, i.e., in every time step the interface is approximated by a line (2D) or a plane (3D) from the volume fraction distribution.

The distribution of the volume fraction is then employed to calculate the f -fluxes to and from interface cells. Since a Cartesian mesh is employed in *FS3D*, this can be done in a split manner and an account of the flux calculation with the PLIC method in *FS3D* is given in [25]. The resulting fluxes are stored for later re-use in the species advection step as explained below.

The simulation of mass transfer at fluid interfaces requires specialized numerical methods in order to capture the occurring physical phenomena. Key issues in the simulation of mass transfer which have to be addressed for obtaining an accurate method are:

- *discontinuity of concentrations* at the interface modeled by Henry's law, i.e. $c^d/c^c = H$,
- simulation of transfer as well as non-transfer species, in particular *no artificial mass transfer*,
- accurate simulation of *local* mass transfer across the interface.

Here, we outline the basic numerical method for dilute species transfer, which is the basis for the simulation of mass transfer accompanied by volume effects as presented in Section 4. We will only give details for those items which are necessary to understand the method for multi-component mass transfer with volume change. For more information on the numerical approach for dilute species transfer, the reader is referred to Bothe and Fleckenstein [4]. A more extended version, also including the simulation of interface contamination and volume effects can be found in the Ph.D. thesis [7].

3.1. Two-scalar approach for species transport

Henry's law leads to a concentration jump of all species at the interface. In order to handle this discontinuity numerically, a two-scalar approach is employed in *FS3D*, i.e., for every single species two scalar fields are used to represent the species concentration, one for each phase. In the numerical method we hence employ the fields

$$\phi_k^c(t, x) = \begin{cases} c_k, & x \in \Omega^c(t) \\ 0, & x \in \Omega^d(t) \end{cases} \quad \text{and} \quad \phi_k^d(t, x) = \begin{cases} 0, & x \in \Omega^c(t) \\ c_k, & x \in \Omega^d(t) \end{cases} \quad (70)$$

for species k . This approach allows for an exact treatment of the one-sided concentration limits at the interface and, hence, for an accurate simulation of species transfer. With the given representation of species concentration, transfer across the interface is treated explicitly. This is done by an exchange term $\Phi_{l,m,n}^k$ which contains the local flux of species k across the interface in a cell with index (l, m, n) and which acts as a sink in one of the fields $\phi_k^i(x)$ and as a source in the other phase. Since species mass is thereby exactly exchanged, this approach is conservative. The computation of the source term $\Phi_{l,m,n}^k$ is explained in more detail in Section 3.2 below.

With the described two-scalar approach, in which the concentration fields are extended by “0” into the respective other phase, it is possible to employ essentially the same geometry-based numerical methods for advection of the concentration fields as used for the volume fraction field f . Doing so, the concentration jump at Σ is kept sharp and a smearing of the species across the interface is prevented, i.e., the interface and the surface of the concentration jump discontinuity coincide throughout a simulation.

To advect a dilute species, first, the fluxes are computed with a higher order upwind scheme employing the MC-limiter [39]. These fluxes, however, are only used for the transport of ϕ_k^c and ϕ_k^d between cells which are entirely contained in Ω^c and Ω^d . To obtain the flux of a species at cell faces adjacent to interface cells, the PLIC fluxes of the volume fraction are used. The flux of species at such a cell face is computed by multiplying the PLIC fluxes by the species concentration at the specific face. For more details, see Bothe and Fleckenstein [4].

Diffusive transport between cells which are entirely contained in one of the bulk phases is done with a standard Finite Volume method and a dimensional (Strang) splitting, i.e., the 3D transport is implemented as a sequence of three one-dimensional transport steps. The diffusive fluxes to and from cells which contain both phases must be corrected, since transport at this step is only inside a phase and, therefore, the “degree of filling” of an interface cell must be taken into account to compute an accurate concentration gradient. To correct for this, the diffusive flux between two cells in a one-dimensional transport step is based on the adjusted concentration gradient

$$\widetilde{\partial_x c} = \gamma_i \frac{\tilde{c}_i - \tilde{c}_{i+1}}{x_{i+1} - x_i} \quad (71)$$

in which the correction factor γ_i has been inserted. This factor takes different values depending on the spatial direction of the one-dimensional transport step. For direction j , the correction factor is computed as

$$\gamma_i^j = \frac{2}{2 - (1 - f^k)|n_j|}, \quad (72)$$

where f^k is the phase fraction of the considered phase in an interface cell, i.e., $f^d = f$ and $f^c = 1 - f$ using the notation employed in the rest of this paper and n_j is the j -th component of the interface normal. This correction is done for diffusion between a pure bulk cell and an interface cell. The heuristic correction factor above has first been employed by Bothe and Fleckenstein [4]. In order to illustrate how this factor works, consider the following two examples for one-dimensional diffusive transport in the continuous phase, where $f^k = 1 - f^d = 1 - f$.

- *Transport in normal direction of the interface:* This case occurs, if the interface normal is aligned with the transport direction of the one-dimensional transport step. Then, since \mathbf{n}_Σ is parallel to the transport direction, $i = j$ in (72) and $|n_j| = 1$. Hence, we get

$$\gamma_i^j = \gamma_i^i = \frac{2}{2 - (1 - (1 - f))|1|} = \frac{2}{2 - f}. \quad (73)$$

The volume fraction f functions as a measure for the position of the interface in this situation. If the interface cell is nearly void of the disperse phase, i.e., $f \approx 0$ and no correction at all is employed, since diffusion between the interface cell and its neighboring cell should be carried out as between two bulk cells. On the other hand, if the considered interface cell contains only a very small fraction of the continuous phase, i.e., $f \approx 1$, a correction factor $\gamma_i^i = 2$ is employed.

- *Transport parallel of the interface:* In this case, \mathbf{n}_Σ is normal to the transport direction and, hence, $|n_j| = 0$ in (72). Therefore,

$$\gamma_i^j = 0 \quad (74)$$

and no correction is applied. This behavior of the correction is exactly as intended, since for the high resolutions usually employed in a DNS, the interface (PLIC-) planes in two neighboring cells are also nearly parallel and, therefore, a correction of the discretization length for the computation of the concentration gradient is unnecessary.

3.2. Unsplit subgrid-scale computation of the mass transfer at the interface

In this section, a brief outline of the flux computation of a transfer species across the interface is given. A detailed description of this method can be found in [4]. For computing the flux at Σ in an interface cell, several problems have to be tackled. In the context of the VOF-method, the most important challenges are the approximation of the correct interface area inside a cell and the approximation of the concentration gradient in normal direction. For dilute species, the species flux at Σ is determined solely by the diffusive flux and, hence, the interface normal concentration gradient. If volume effects are considered an additional convective flux appears, known as the Stefan flux in the context of phase change problems. A discussion on when this effect is relevant can be found in [4]. The numerical implementation of this additional convective fluxes is described below in Section 4. Here, we focus on the accurate approximation of the interface normal gradient of the species concentration.

To approximate the concentration gradient in normal direction in an interface cell, first, the centroid x_Σ of the PLIC element is computed. A concentration at this centroid is computed by linear extrapolation of the species concentration from the donating phase onto the centroid and then applying Henry's law, which gives the concentration c_Σ^{acc} at x_Σ but at the accepting phase side. Note that a (linear) extrapolation to obtain an improved concentration value at the interface is required for conjugated mass transfer, where a noticeable concentration gradient is present in both phases. Secondly, two concentration values c_1 and c_2 in the bulk phase are computed at points A_1 and A_2 as given in Fig. 2, i.e., at planes parallel to two coordinate axes. With c_Σ^{acc} , c_1 and c_Σ^{acc} , c_2 two normal derivatives $(\partial_{\mathbf{n}^d} c)_1$ and $(\partial_{\mathbf{n}^d} c)_2$ can be calculated. These derivatives can be either computed with a linear approximation or with a subgrid-scale method which allows for an increased accuracy for a given resolution of the concentration boundary layer. We note that all results in this paper have been obtained with such a subgrid-scale approach, but for the sake of brevity, the reader is referred to [4] for a detailed description. After these derivatives are computed, the concentration gradient at x_Σ which is used to compute the mass flux is calculated as

$$\partial_{\mathbf{n}^d} c|_\Sigma = (1 - f)(\partial_{\mathbf{n}^d} c)_1 + f(\partial_{\mathbf{n}^d} c)_2 \quad (75)$$

if the direction of the mass flux points into the continuous phase and as

$$\partial_{\mathbf{n}^d} c|_\Sigma = f(\partial_{\mathbf{n}^d} c)_1 + (1 - f)(\partial_{\mathbf{n}^d} c)_2 \quad (76)$$

if species is transferred from the continuous phase to the disperse phase.

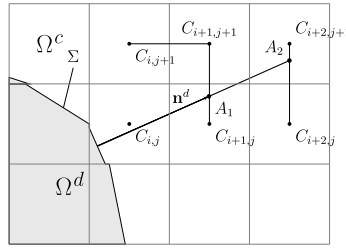


Fig. 2. Unsplit approximation of the concentration gradient at the interface.

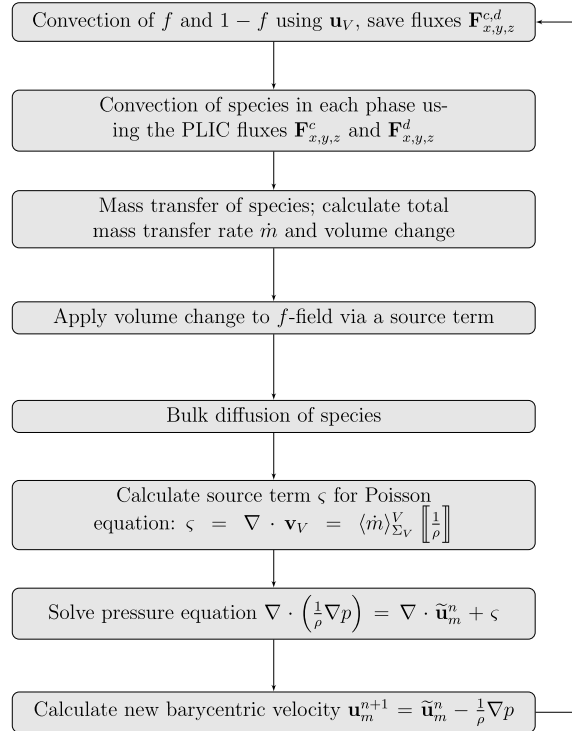


Fig. 3. Sequence of operations for mass transfer with volume effect.

4. Numerical method for multi-component mass transfer accompanied by volume effects

This section presents the numerical scheme for the averaged equations derived in Section 2.2. This algorithm is an extension of the algorithm for mass transfer of dilute chemical species. As such, for vanishing mass fraction of the species and vanishing volume change due to mass transfer, this extension falls back to the dilute case described before and also the bulk diffusion of species and the calculation of the diffusive flux across the interface are computed with the schemes presented in Section 3. The complete scheme is shown in Fig. 3, but several remarks are in order here. First, in FS3D the momentum equation is solved in the form

$$\partial_t \mathbf{v} + \mathbf{v} \cdot \nabla \mathbf{v} = \frac{1}{\rho} (\nabla p + \text{div} \mathbf{S} + \mathbf{f}_\Sigma) + \mathbf{g}. \quad (77)$$

For the computation of surface forces \mathbf{f}_Σ in FS3D, the average density $\bar{\rho} = \frac{1}{2}(\rho^d + \rho^c)$ is employed, cf. Rieber [25], since using the mixture density would result in large accelerations in control volumes which are nearly void of liquid. This approach has been suggested by Brackbill et al. [5] and the reader is referred to this paper for more details regarding computation of surface forces. For momentum transport, the exact local density $\rho = \sum_i \rho_i$ in the present method is only used to calculate the specific pressure $\nabla p / \rho$. In order to take gravitational effects into account, a Boussinesq approximation is employed in which the exact local mixture density is used.

4.1. Order of the transport steps

The scheme presented in Fig. 3 reflects an operator split approach to mass transfer and hydrodynamics. However, the order of the operations is not arbitrary. Besides obviously necessary operational sequences, e.g. calculating the source term for the pressure equation before solving the pressure equation, there are less obvious reasons for the specific order in this scheme. In particular, the volume change of phase Ω^k , which is implemented as a source term in the Volume-of-Fluid equation (32), must be applied after mass transfer of the components, but before any other transport step of the components is carried out. Otherwise, over- or undershoots of species concentration would occur as can easily be understood for mass transfer of a pure gas phase into a liquid. Indeed, consider the following two orders of operation: First, the sequence *mass transfer* \rightarrow *species diffusion* \rightarrow *volume change* and, second, the order presented above, i.e. *mass transfer* \rightarrow *volume change* \rightarrow *species diffusion*. In the first case, mass transfer is computed and the concentration of the component in phase Ω^k is reduced. Since the volume fraction of the phase is kept constant during this operation, this leads to a non-physical, decreased concentration in the interface carrying cell for the gas phase. Next, due to the lower concentration in the grid cell under consideration, species is fluxed from the neighboring gas phase into this cell during diffusional transport. Therefore, when the phase fraction is then adjusted according to the transferred mass, the concentration of the gas component in phase Ω^k becomes larger than the density in the neighboring gas phase, which is unphysical. On the other hand, for the second order of operations, the phase volume is adjusted for the volume change directly after the mass transfer step, thus leading to the correct concentrations. In the specific special case of a pure gas, this concentration is actually constant and the diffusive fluxes vanish, which leads to a physically reasonable result.

4.2. Transport of the volume fraction field

The balance equation for the volume fraction f has been derived in Section 2.2.1 and is recalled here:

$$\partial_t f + \langle \mathbf{v} \rangle_{V^d} \cdot \nabla f = \frac{\langle \dot{m} \rangle_{\Sigma}^V}{\rho^d}. \quad (78)$$

As noted in Section 2.2.1, the velocity field $\langle \mathbf{v} \rangle_{V^d}$ is approximately divergence free, hence the solution of (78) can be split into applying a source or sink according to volume change, by which the total phase volume is altered, and a volume conservative advection with the velocity $\langle \mathbf{v} \rangle_{V^d}$. This splitting is well suited for standard PLIC-based advection schemes for incompressible flow, since here also divergence free velocity fields are used.

Despite this theoretical advantage, the phase averaged velocity $\langle \mathbf{v} \rangle_{V^d}$ is not well-suited for transport of a quantity on an Eulerian mesh. First, since in a finite volume setting $\langle \mathbf{v} \rangle_{V^d}$ is the average velocity inside the dispersed phase within a cell – not inside the entire cell – it cannot be discretized naively as it corresponds to the barycenter of the specific phase inside a control volume. Second, the used discretization with a staggered grid, where the velocities are located at cell faces, requires a solenoidal extension of this phase averaged velocity to all cell faces of an interface cell which are not fully wetted by the fluid of phase Ω^d . By the latter, we mean cell faces which are in contact with both phases based on the PLIC approximation of Σ . Finding such an extension is not trivial and requires to solve an additional Poisson equation in all cells with $f^d < 1 - \varepsilon$ in such a way that the disperse phase velocity is not changed at cell faces which are fully wetted by the dispersed phase and its extension to all other cell faces is divergence free. Due to these reasons, the phase averaged velocity $\langle \mathbf{v} \rangle_{V^d}$ in Equation (32) is replaced by the volume averaged velocity \mathbf{v}_V in the advection step. This has the advantage that \mathbf{v}_V and $\langle \mathbf{v} \rangle_{V^d}$ coincide for all faces which are completely wetted by the fluid of phase Ω^d as a result of the derivation of these velocities.

At this point, a remark is at order: Note that it is possible to express $\langle \mathbf{v} \rangle_{V^d}$ in terms of the volume averaged velocity as

$$\langle \mathbf{v} \rangle_{V^d} = \mathbf{v}_V + (1 - f)\mathbf{v}_r, \quad (79)$$

and derive a transport equation for f based on \mathbf{v}_V , resulting in

$$\partial_t f + \text{div}(f\mathbf{v}_V) = \frac{\langle \dot{m} \rangle_{\Sigma}^V}{\rho^c}; \quad (80)$$

cf. Ma and Bothe [18] for details on the separation of the velocities as done in (79). Since this equation is in conservative form, we see that a volume fraction change according to the source term on the right-hand side of the equation occurs, which is inconsistent with the originally derived change of phase volume. The reason for this inconsistency is that the volume fraction f is derived from the phase indicator of the disperse phase, which is zero in Ω^c . However, in the (formal) derivation of the last equation, f is treated as a quantity which is evenly distributed in an entire cell. For this reason, we do not follow the latter approach here. Instead, as stated above, we employ (78), but with $\langle \mathbf{v} \rangle_{V^d}$ replaced by \mathbf{v}_V .

The problem explained above does only occur in interface cells. Within the bulk phase, volume averaged and phase averaged velocities coincide and the convective fluxes can easily be computed with a higher-order upwind scheme. The resulting fluxes are then stored for the convective transport of ϕ_k^d , the dispersed phase field of species k . To obtain the convective fluxes for the transport of all components in the continuous phase, the quantity $1 - \tilde{f}$ is convected using the PLIC method and the volume averaged velocity, where \tilde{f} denotes the volume fraction distribution of the dispersed phase prior to the advection of the volume fraction.

4.3. Divergence correction

Standard PLIC-based advection uses the non-conservative form given by Equation (69) to transport the f -field. Without volume change, i.e. for divergence free velocity fields, this is equivalent to the conservative form (31). However, even for a discretely divergence free velocity field, a dimensionally split advection scheme based on a conservative transport equation for f leads to over- and undershoots inside the bulk phase, where the volume fraction should be exactly $f = 1$. This so-called splitting error must be corrected for, cf. Rieber [25] for details. In order to do so, the term $f \partial_i u_i$ is added in every one-dimensional transport step on both sides of the split volume fraction equation,

$$\partial_t f + u_i \partial_i f = 0, \quad (81)$$

in which u_i is a component of the divergence free velocity field \mathbf{v} . Then, with the right-hand side adjusted for errors due to a dimensionally split scheme, in the n -th time step, the f -advection becomes [25]

$$\frac{f^* - f^n}{\delta t} + \frac{\partial(f^n u_x^n)}{\partial x} = \frac{1}{2}(f^n + f^*) \partial_x u_x^n, \quad (82)$$

$$\frac{f^{**} - f^*}{\delta t} + \frac{\partial(f^* u_y^n)}{\partial x} = \frac{1}{2}(f^* + f^{**}) \partial_y u_y^n, \quad (83)$$

$$\frac{f^{n+1} - f^{**}}{\delta t} + \frac{\partial(f^{**} u_z^n)}{\partial x} = \frac{1}{2}(f^{**} + f^{n+1}) \partial_z u_z^n, \quad (84)$$

where u_x , u_y and u_z are the x -, y - and z -components of the velocity \mathbf{v} , respectively. Now, since $\langle \mathbf{v} \rangle_V$ exhibits a physically meaningful (non-vanishing) divergence in mesh cells carrying interface if volume change is considered, the divergence correction on the right-hand sides of (82)–(84) must be adjusted in interface cells as they reintroduce a source/sink for the volume fraction. This is done by adding all correction factors of the one-dimensional transport steps and subtracting the sum after all one-dimensional transport steps have been executed, cf. Schlottke [30]. If this adjustment is skipped, volume change would be performed twice: via the source term $\langle \dot{m} \rangle_\Sigma^V / \rho^d$ and during f -advection. Let us also note in passing that if no volume change is considered, canceling the divergence correction after advecting the volume fraction does not change the f -transport, since the velocity is then divergence free and the sum of the right-hand sides of (82)–(84) converges to zero for higher resolutions. In other words, the above described modification to treat volume change is also applicable if volume change does actually not appear.

5. Validation of the numerical method

In this section, the developed method is validated by comparison to an analytical 1D test case and by comparison to an exact solution in 3D. Here, by an “exact solution” we mean a reference solution of the species transfer obtained with an analytical solution of the flow field around a rising gas bubble in creeping flow and a finite difference approximation of a parabolized version of the species equation, where an extremely high resolution has been used. The procedure of solving this parabolized mass transfer problem is described in detail in [4].

5.1. Comparison to 1D analytical solution

First, we compare a 1D simulation with *FS3D* to an analytically solvable test case. Similar validation cases have been previously used by, e.g., Welch and Wilson [40] for the validation of numerical methods for evaporation.

For this validation case, we consider mass transfer from a (pure) gas phase into a semi-infinite liquid phase. Initially, the interface between Ω^G and Ω^L is at position $x = x_0$. The concentration of the single component inside Ω^G remains constant throughout the simulation. Then, under the assumption that the transferred gas is highly diluted in the liquid phase, the equation for the species concentration c in the liquid phase can be written as

$$\begin{cases} \partial_t c = D \partial_x^2 c, & x > 0, t > 0, \\ c(0, x) = 0, & x > 0, \\ c(t, 0) = c^G / H, & t > 0, \end{cases} \quad (85)$$

where the origin of the coordinate system moves with the interface position and H is the Henry coefficient. The time dependent solution to this diffusion equation is given by [6]

$$c(t, x) = -\frac{c^G}{H} \operatorname{erf}\left(\frac{x}{2\sqrt{Dt}}\right) + c^G / H. \quad (86)$$

With this species distribution in the liquid phase, we obtain

$$\frac{\partial c}{\partial \mathbf{n}_\Sigma} = -\frac{c^G}{H\sqrt{\pi D}} \frac{1}{\sqrt{t}}, \quad (87)$$

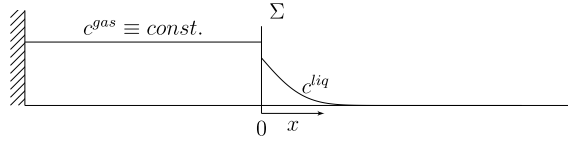


Fig. 4. Setup of the validation case.

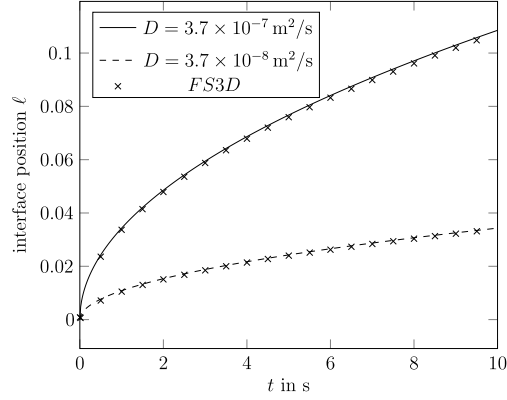


Fig. 5. Interface position vs. time.

the normal derivative of the transfer species at the interface. Taking this concentration derivative, we can finally compute the velocity of the interface as

$$V_{\Sigma} = -D \frac{c^G}{H\sqrt{\pi D}} \frac{1}{\sqrt{t}}, \quad (88)$$

i.e. the traveled length ℓ of the interface is

$$\ell = 2 \frac{c^G}{H} \sqrt{tD/\pi}. \quad (89)$$

A principal sketch of the validation case some time t after the initial time t_0 is given in Fig. 4.

To validate the numerical method, we use the position of the interface as given by Equation (89) and compare with the simulation results from FS3D. These simulations employ as diffusion coefficients $D = 3.7 \times 10^{-7} \text{ m}^2/\text{s}$ and $D = 3.7 \times 10^{-8} \text{ m}^2/\text{s}$ and a Henry coefficient of $H = 2$. As the analytical solution has been obtained for a semi-infinite domain, ample distance between the interface position and the right domain boundary (as in Fig. 4) has been chosen. The comparison of analytical and numerical solution of the problem up to the final time $t_{fin} = 10 \text{ s}$ is presented in Fig. 5. From this figure, we see that a very good agreement between the VOF-based simulation and the exact solution is reached. The minor, slowly growing deviation between numerical and analytical solution is due to the fact that during the motion of the interface, cells with very small phase fractions occur and in some cases, the mass flux into or from the small phase fraction is larger than the physically possible value, i.e. it would to a concentration either being negative or a larger than the Henry law allows. In this case, the flux is limited to the physically maximum possible value which introduces a small systematic error. It is important to note that this problem is visible only in 1D computations, since the occurrence of several grid cells with interface and with only a very small fraction of one of the phases is very unlikely. We indeed did not observe this in any 3D computation.

5.2. Comparison to 3D test case

5.2.1. Semi-analytical solution of the mass transfer from a gas bubble in creeping flow

In order to obtain suitable validation data for the shrinking of a rising bubble, an accurate solution of the full species equations is necessary. However, no analytical solution to this problem is available. Therefore, we derive here a combined analytical/numerical method to solve the mass transfer around a rising bubble. To do so, the well-known Hadamard–Rybczynski solution for the flow around a spherical fluid particle in creeping flow, see [10] and [27], is used as the velocity field. Employing the analytical velocities, the rotationally symmetric stationary species equation is solved numerically with a finite difference approach. Since the computation of the solution is numerically inexpensive, the accuracy can be increased to any requested level.

In spherical coordinates and in a reference frame moving with the barycenter of the particle, the Hadamard–Rybczynski velocity field is given by

$$v_r = -U_p \left(1 - \frac{1.5\eta_p/\eta_c + 1}{\eta_p/\eta_c + 1} \frac{1}{r/R} + \frac{\eta_p/\eta_c}{\eta_p/\eta_c + 1} \frac{1}{(r/R)^3} \right) \cos \theta, \quad (90)$$

$$v_\theta = U_p \left(1 - \frac{1.5\eta_p/\eta_c + 1}{\eta_p/\eta_c + 1} \frac{1}{2r/R} - \frac{\eta_p/\eta_c}{\eta_p/\eta_c + 1} \frac{1}{2(r/R)^3} \right) \sin \theta, \quad (91)$$

where v_r and v_θ are the radial and the tangential components, respectively, of the velocity around a fluid sphere. The ratio r/R denotes the dimensionless distance to the interface and η_p/η_c is the ratio of the particle and continuous phase dynamic viscosity. Furthermore, U_p is the rise velocity of the fluid particle, which can be calculated as

$$U_p = \frac{2}{3} \frac{\rho_p - \rho_c}{\eta_c} g R^2 \frac{1 + \eta_p/\eta_c}{2 + 3\eta_p/\eta_c} \quad (92)$$

by equating buoyancy force and drag force at the interface.

Assuming rotational symmetry, the stationary species equation in the continuous phase is given by

$$v_r \frac{\partial c}{\partial r} + v_\theta \frac{1}{r} \frac{\partial c}{\partial \theta} = D \left(\frac{1}{r^2} \frac{\partial}{\partial r} \left(r^2 \frac{\partial c}{\partial r} \right) + \frac{1}{\sin \theta} \frac{\partial}{\partial \theta} \left(\sin \theta \frac{\partial c}{\partial \theta} \right) \right). \quad (93)$$

Now, species transport from a sphere rising with the velocity field given above can be simplified. As the tangential component of the analytical velocity vanishes only at the front and rear pole of the fluid particle ($\theta = 0$ and $\theta = \pi$, respectively), diffusive transport of species along the θ -direction can be neglected due to good mixing along streamlines. Hence, we obtain the parabolized form

$$\frac{\partial c}{\partial \theta} = \frac{1}{\text{Pe}} \left(\frac{1}{\tilde{r}} \frac{\partial}{\partial \tilde{r}} \left(\tilde{r}^2 \frac{\partial c}{\partial \tilde{r}} \right) \right) - \tilde{r} \frac{\tilde{v}_r}{\tilde{v}_\theta + \varepsilon} \frac{\partial c}{\partial \tilde{r}} \quad (94)$$

of the species equation, where the tangential velocity \tilde{v}_θ has been replaced by $\tilde{v}_\theta + \varepsilon$ for a fixed small $\varepsilon > 0$ to ensure that no singularity occurs at the poles of the particle. Note that in this equation a rescaling with $\tilde{r} = r/R$, $\tilde{v}_r = v_r/U_p$ and $\tilde{v}_\theta = v_\theta/U_p$ has been performed. The Péclet number above is then given by $\text{Pe} = U_p R/D$. The variable θ can now be viewed as a pseudo-time since at every θ^n the right-hand side in (94) only depends on the state at θ^n . To solve equation (94) numerically, a homogeneous Neumann boundary condition has been used at the outer boundary. However, in all cases to follow, a sufficiently large distance of the sphere to the domain boundary has been employed such that no wall-effect is observed. To obtain a solution of the mass transfer problem, the species transport is only solved for in the continuous phase since the dispersed phase can be considered well-mixed.

5.2.2. Mass transfer from a gas bubble in creeping flow with volume effect

For a 3D validation of the algorithm which incorporates volume effects into mass transfer, we revisit the semi-analytical test case for mass transfer based on the Hadamard–Rybczynski solution. The semi-analytical validation case for mass transfer without additional effects gives an estimate of the local and global Sherwood numbers for stationary mass transfer from a rising spherical bubble in creeping flow. Now, in order to predict the change of volume due to mass transfer, we compute the rate of change of the dispersed phase volume based on the Sherwood number from the semi-analytical solution.

Recall that $\text{Sh} = \frac{1}{|\partial V|} \int_{\partial V} \text{Sh}_{loc} dA$ and the local Sherwood number is given as

$$\text{Sh}_{loc} = - \frac{\partial c}{\partial \mathbf{n}_\Sigma} \bigg|_\Sigma \bigg/ \frac{c_\Sigma - c^\infty}{d} = - \frac{\partial \rho^c}{\partial \mathbf{n}_\Sigma} \bigg|_\Sigma \bigg/ \frac{\rho_\Sigma^d/H - \rho^\infty}{d}, \quad (95)$$

where H is the Henry coefficient, M is the molar mass of the transfer component and ρ^c, ρ^d the component's density in continuous and disperse phase, respectively. For a vanishing density of the transfer component “at infinity”, i.e., $\rho^\infty = 0$, and for a single component gas bubble, the normal density derivative at the interface of the transfer component is

$$\frac{\partial \rho^c}{\partial \mathbf{n}_\Sigma} = -\text{Sh}_{loc} \frac{\rho^d}{Hd}. \quad (96)$$

Assuming diluteness of the transfer component in the continuous phase, the rate of change of the dispersed phase mass m is computed via

$$m'(t) = D \int_{\partial V} \nabla \rho \cdot \mathbf{n}_\Sigma dA = -D |\partial V| \text{Sh} \rho^d / (Hd). \quad (97)$$

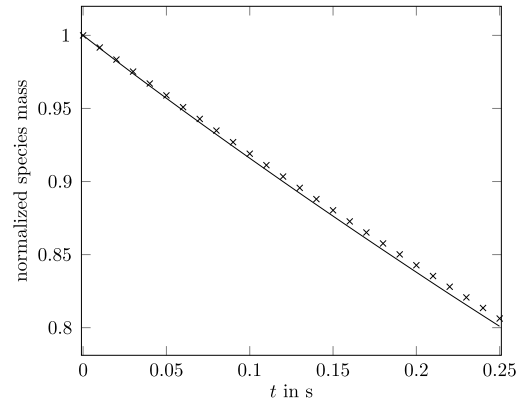
Using $m(t) = \int_V \rho^d dV = \rho^d |V(t)|$, which is valid for a constant density, and employing $V = 4/3\pi r^3$, we get the ordinary differential equation

$$r'(t) = - \frac{1}{2H} \frac{\text{Sh}(r(t))}{r(t)} \quad (98)$$

Table 1

Material properties for mass transfer from air bubble in creeping flow.

Phase	Density ρ (kg m ⁻³)	Dyn. viscosity η (mPa s)	Diffusivity D (m ² s ⁻¹)	Schmidt number Sc (ν/D)
Gas	1.2	1.8×10^{-2}	2×10^{-5}	0.75
Liquid	1245	460	1.48×10^{-6}	250

**Fig. 6.** Normalized total mass of gas phase vs. time. Dispersed phase mass normalized by initial value. Crosses indicate semi-analytical solution; continuous line: simulation result from FS3D.

for the radius of the sphere. Note that Sh depends here on the Reynolds and Schmidt number of the considered system and, thus, on the radius r . Hence, an analytical solution for a rising bubble is not possible and the Equation (98) will thus be solved numerically. To this end, the parabolized Equation (94) is solved and used to compute the integral Sherwood number and based on this, an update of the radius.

To compare with this reference solution, mass transfer from a single component gas bubble has been simulated using the material properties given in Table 1. The continuous-phase diffusivity of the transfer component has been chosen such that $Sc = 250$ and a rather large Henry coefficient $H = 5$ has been employed, which leads to increased mass transfer and, hence, a faster dissolution of the bubble. In the simulation with FS3D, a bubble with the initial diameter of $d_B = 4$ mm has been simulated in a computational domain of dimensions $2.4 \text{ cm} \times 1.2 \text{ cm} \times 1.2 \text{ cm}$ and the bubble center is placed at $(1.2 \text{ cm}, 0 \text{ cm}, 0 \text{ cm})$, i.e., a symmetry condition is used and only a quarter of the bubble is simulated. The computational domain is resolved uniformly with $192 \times 96 \times 96$ cells.

The parabolized species Equation (94) determines the stationary mass transfer from a sphere. In order to have comparable solutions, mass transfer without volume change and with a constant species density in the gas phase has been simulated with FS3D until a steady state is reached. Starting from this steady state solution at time t_0 , conjugate mass transfer with volume change is simulated for a physical time span of 0.25 s. At $t = t_0$ the bubble rises with a velocity of 3.0 cm/s, while the exact rise velocity predicted by the Hadamard–Rybczynski solution is approximately 3.5 cm/s for the considered material parameters. To adjust for this discrepancy, the rise velocity from the Direct Numerical Simulation is used in (90) and (91) of the validation case to compute mass transfer. Note at this point that the Hadamard–Rybczynski solution first of all provides the velocity fields inside and outside of a translating spherical fluid particle which is the combined with a force balance in also to also provide the rise velocity. But if a rise velocity corresponding to sufficiently small Re is given, a consistent creeping flow field is obtained.

The resulting decrease of disperse phase mass/volume from a simulation with FS3D and the validation case discussed before is depicted in Fig. 6. After a total simulated physical time of 0.25 s, the volume/mass has decreased to 80.1% of its initial value in the Direct Numerical Simulation and to 80.6% of the initial value in the semi-analytical solution. This corresponds to a relative deviation of 0.7% of the volume at the end of the simulation.

Similar to the procedure above, Equation (98) can also be solved with the Sherwood number given by a correlation. This has been done with the correlation

$$Sh = 2 + 0.651 \frac{Pe^{1.72}}{1 + Pe^{1.22}}, \quad (99)$$

valid for $Re \rightarrow 0$ and $Sc \rightarrow \infty$ [21], which is based on a numerical computation of mass transfer at a spherical bubble and gives a good estimate of the Sherwood number. Since this correlation yields very similar Sherwood numbers compared to the numerical method, deviations from the validation case can be attributed to the computed volume effects. At t_0 , the integral Sherwood numbers from simulation and the correlation differ by only 0.03% with a higher Sherwood number yielded by the DNS.

If the rise velocity for this simplified validation case is computed based on the terminal rise velocity of the Hadamard–Rybczynski solution, including a correction factor such that the initial rise velocities are equal, we are able to compute a

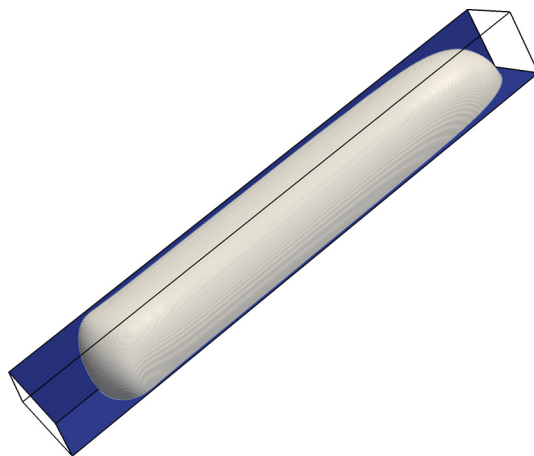


Fig. 7. Taylor bubble in computational domain.

compound error. After 0.25 s of simulation, the solution of the ordinary differential equation yields a decrease of the total mass/volume to 79.9% of the initial value. This corresponds to a deviation of 0.26% of the simulation from the validation case and, hence, a very good agreement is reached.

6. Applications of the numerical method

The numerical method described above represents a further step towards computation of the multi-physics accompanying mass transfer across fluid interfaces. This method has been applied to simulate two prototypical examples, where the main aim is to provide a proof of principle rather than to fully explore the underlying case – the latter is outside the scope of the present paper and requires further studies.

6.1. Shrinking of a Taylor bubble in a square channel

In this section, the volume effect of mass transfer on a rising Taylor bubble is investigated. The hydrodynamics of a rising Taylor bubble has been validated for FS3D in [20], where the same material parameters for the hydrodynamics are employed as here. The numerical setup corresponds to a system of air and a liquid mixture consisting of water and glycerol; the material parameters are $\eta^{gas} = 20 \times 10^{-6}$ kg/ms and $\eta^{liq} = 28.54 \times 10^{-3}$ kg/ms for the viscosity and $\rho^{gas} = 1.3$ kg/m³, $\rho^{liq} = 1195.6$ kg/m³ for the density of the fluids. The surface tension at the air–liquid interface is given as $\sigma = 66.69 \times 10^{-3}$ N/m. In the experiment which has been used to validate the numerical code, a square channel with a cross sectional area of 2.0 mm \times 2.0 mm is considered. Here, however, only a quarter of this channel is simulated so that the simulation domain has a lateral extent of 1.0 mm and a length of 8.0 mm, which is resolved with $512 \times 64 \times 64$ grid cells. At the lateral walls the no-slip condition is applied, at the lateral symmetry boundaries the appropriate symmetry condition is employed and at the left wall an inflow condition with a fixed inflow velocity of $u_{inflow} = 17.6$ cm/s is used. A homogeneous Neumann boundary condition for the velocity fields is applied at the right wall. To illustrate the computational domain and the Taylor bubble inside, the contour of the bubble interface in the simulation domain is depicted in Fig. 7. The employed symmetry planes are solidly colored and the bubble rises to the right.

Since the simulation of Taylor bubbles even without additional physics is itself numerically challenging, momentum and mass transfer have been simulated first without volume effect until the quasi-steady state is reached. At this state the simulation has been restarted with the accompanying volume effect switched on. Two simulations of mass transfer have been performed. In both simulations, the gas phase has been assumed to be a single component gas and only the liquid side diffusivity of the gas component has been varied. In the low diffusivity case, a diffusion coefficient of $D = 2.0 \times 10^{-9}$ m²/s has been used, while $D = 2.0 \times 10^{-8}$ m²/s has been employed in the corresponding high diffusivity case. The Henry coefficient of the chemical species has been set to $H = 1.203$, corresponding to the Henry coefficient of CO₂ in an air/water system under standard conditions. This is in accordance with the considered small diffusion coefficient, which is also the diffusion coefficient of CO₂ in water. The total simulation time for mass transfer with volume change is 0.1 s.

The resulting change of bubble volume vs. time is shown in Fig. 8. As expected, the volume of the Taylor bubble shrinks faster for the case with the higher diffusivity. As can be seen from the graph in Fig. 8, the shrinking rate is almost linear in both cases. Due to the narrow domain, this shrinking mainly leads to a shortening of the bubble as can be seen in Fig. 9. Let us note that the computations employ a window-technique by which the computational domain is co-moving with the bubble's center. This allows for simulation over longer time frames with moderate computational domain size without the bubble leaving this domain.

The shrinking of the bubble depicted in this figure is not uniform at the interface but depends on the local mass transfer which may vary considerably. To investigate the local mass transfer, Sherwood numbers at the interface of the

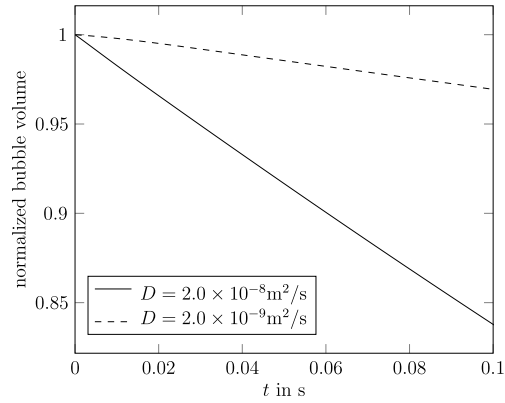


Fig. 8. Normalized bubble volume vs. time for mass transfer in Taylor flow.

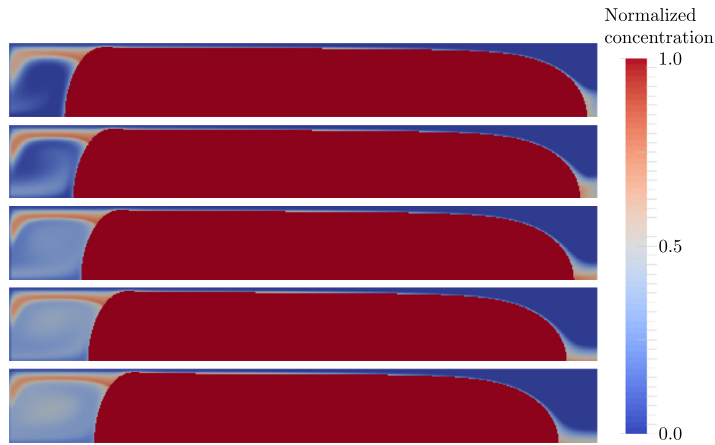


Fig. 9. Cross section of concentration fields around a Taylor bubble for times $t = 0.01$ s, 0.03 s, 0.05 s, 0.07 s and 0.09 s after start of mass transfer computation at developed hydrodynamics; $D = 2.0 \times 10^{-8} \text{ m}^2/\text{s}$.

simulated Taylor bubble are displayed in Fig. 10 for three different visual perspectives. The local Sh presented here have been calculated based on the diameter of the channel. The figure shows that simplifying assumptions regarding mass transfer are difficult to make as the local Sherwood number varies in rise direction as well as in circumferential direction. The lowest Sh are observed at the rear of the bubble where flow separation occurs. The largest values of Sh occur at the front of the bubble, where the increase of the bubble diameter is strongest. Starting from this maximum, a decrease of the local Sherwood number can be observed both in upflow and downflow direction. At the tip of the bubble, species is concentrated by the bubble movement, as can be seen in the concentration fields given in Fig. 9. This leads to a locally reduced mass transfer.

In downflow direction, the decrease of the local Sherwood number is not uniform, but higher values of Sh appear in regions of the interface which are closer to the walls. This difference is caused by the flow around the Taylor bubble. In the midsection of the bubble the diameter increases slightly and leads to a tangential flow as sketched in Fig. 11. Hence, the species boundary layer becomes thinner, causing a steeper concentration gradient.

6.2. Competing mass transfer in a multi-component gas bubble

Except under specific experimental conditions, mass transfer at fluid interfaces must always be considered as multi-component mass transfer, especially in industrial applications where conditions cannot be as tightly controlled as in a laboratory environment. Both, species being transferred from the gaseous phase to the liquid phase, and species being transferred in the opposite direction directly affect the volume of a bubble. If realistic mass transfer is to be investigated with numerical methods, such a competing mass transfer must be taken into account.

Here we intend to show the ability of the presented method to capture competing conjugate multi-component mass transfer, i.e., conjugate mass transfer of several species where the disperse phase volume is dependent on all transfer species. In order to do so, we simulate multi-component mass transfer at a 1 mm gas bubble which is initially composed of carbon dioxide and at rest. During the simulation, the bubble rises in water which contains dissolved oxygen and nitrogen as transfer species. Similar setups have been studied before experimentally by, e.g., Tomiyama et al. [38]. The experiments

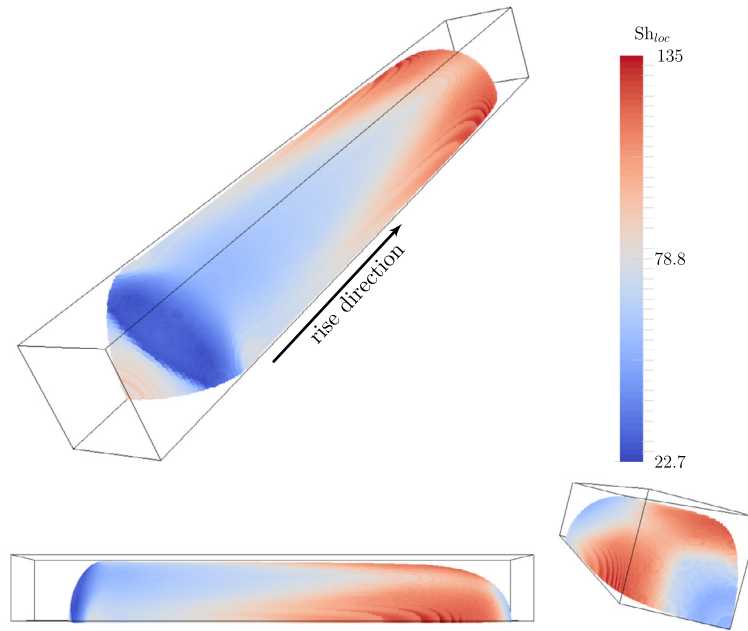


Fig. 10. Local Sherwood numbers at the interface of the Taylor bubble at the beginning of the simulation. Top left: rear view. Bottom left: Lateral view; bubble rising to the right. Bottom right: Front view; bubble rising towards the observer.

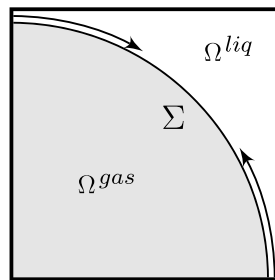


Fig. 11. Schematic view of circumferential flow in a cross section at the middle of the Taylor bubble.

Table 2

Material properties for competing mass transfer at a rising gas bubble.

	c_0^d	c_0^c	H
CO ₂	4.464×10^{-2} mol/l	0	1.2
N ₂	0	0.51×10^{-3} mol/l	67.0
O ₂	0	0.27×10^{-3} mol/l	31.5

presented in this paper show that initially pure gas bubbles rising in mixtures attain a quasi-stationary state, where the internal composition of the disperse phase is in equilibrium with the ambient fluid mixture and the bubble volume is constant. However, the described final state is only reached after relatively long times, i.e., several seconds, which is presently not feasible in a DNS. To reduce the necessary simulation time to see an effect, the liquid side diffusion coefficients of the gases have been increased by a factor of 10 compared to the physical properties at standard conditions, while their ratio has been held constant. The initial concentrations and the Henry constants used in the subsequent applications are given in Table 2.

We simulated the rise of an initially spherical bubble of 0.8 mm diameter with competing mass transfer. The computational domain is a box of size 0.8 cm \times 0.2 cm \times 0.2 cm, using a mesh of 512×256^2 grid cells. The simulations are performed using two symmetry planes, i.e. only a quarter of the bubble is computed.

The simulation result is summarized by Fig. 12, in which bubble composition and volume is plotted versus time. From this figure, we can see that the bubble volume decreases almost linearly in the beginning of the simulation as the concentration of carbon dioxide in the bubble drops and the fraction of the other two species is still marginal. With increasing

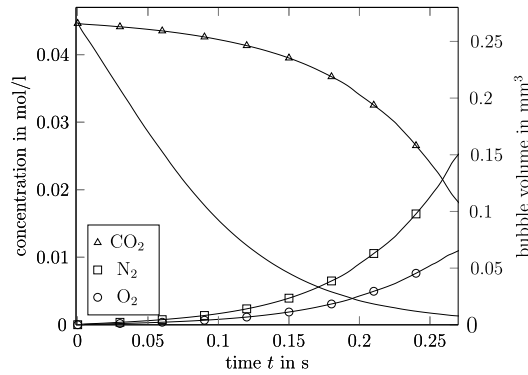


Fig. 12. Disperse phase concentration of transfer components and bubble volume vs. time for competing mass transfer at a rising gas bubble.

simulation time the composition of the bubble changes significantly and, consequently, the effect of CO_2 transfer on bubble volume becomes less influential as its concentration inside the bubble decreases.

At later stages of the simulation the disperse phase is mainly composed of nitrogen and oxygen and the shrinking of the gas bubble is markedly slowed down. Both features are also observed in the experiment. A quasi-stationary asymptotic state with a constant bubble volume is, however, not attained. In order for this to be feasible, additional multi-physics has to be included in the model and, of course, in the numerical method. The most important issues in this respect are: (i) a description of the gas phase as a compressible medium with an appropriate equation of state such as the ideal gas law (for mixtures); (ii) a treatment of the liquid phase which allows for non-zero divergence of the barycentric velocity in accordance to a mixture density; (iii) treatment of pressure-controlled settings rather than volume-controlled ones (note that zero divergence in the bulk phases and mass transfer with volume effects is incompatible to a fixed total volume for a closed system); (iv) evaporation of the liquid phase into the gas phase which is especially relevant in case of a dissolving pure gas bubble into a degassed liquid; (v) inclusion of cross-diffusion effects. These issues shall be investigated in future work. For more detail on the multi-physics accompanying mass transfer from fluid particles see [2].

7. Summary and conclusions

In this paper a numerical method for multi-component mass transfer with volume effects at dynamically deforming interfaces has been presented. The main focus of the article is the rigorous derivation of the underlying equations which allow for a description of local volume change, building on the Volume-of-Fluid method, and the implementation and validation of the corresponding numerical method. Central to this VOF-based approach is a one-field formulation of the incompressible Navier–Stokes equations accounting for volume effects, which is derived using spatial averaging techniques. The numerical implementation of this one-field formulation couples mass and momentum transfer via a local source term in the pressure equation. This source term depends on the local volume effect induced by mass transfer across the interface. To compute the local volume change, the diffusive as well as the convective contribution (Stefan flow) are considered, where the convective part of mass transfer is calculated based on the diffusive fluxes of all transfer species across the interface. The numerical method is conservative regarding species mass and the approach to mass transfer employs an unsplit two-scalar method, which allows to represent the one-sided concentration limits of species at the interface exactly.

The numerical method is validated by comparison to two test cases. First, an analytical solution of a one-dimensional so-called sucking problem is employed. The second validation uses a comparison to a semi-analytical solution of mass transfer in 3D, based on the Hadamard–Rybczynski solution for the velocity around a spherical fluid particle in creeping flow, combined with the numerical solution of the species equations in an appropriately parabolized form in the exterior of the shrinking gas sphere. A very good agreement of the numerical results with the reference solution has been obtained in both validation cases.

The validated approach is applied to the dissolution of a CO_2 Taylor bubble rising in a square mini-channel. For this case, local Sherwood numbers at the bubble have been obtained which show that mass transfer is non-uniform along the interface. This result demonstrates the potential of DNS of mass transfer to investigate local processes in interface vicinity.

Finally, the method has been applied to multi-component mass transfer at a rising gas bubble. The simulation results prove that the presented method is able to capture volume effects with several simultaneous transfer components and different transfer directions. However, a simple example also shows that the incompressible model setting does not provide a mechanism which drives the system to a quasi-stationary state with a constant bubble volume as observed in experiments. Specifically on this point, further investigations are necessary to develop a mathematical model which allows for a sufficiently accurate representation of all the phenomena observed in experiments.

In future work, the presented method will be used and expanded to study further multi-physics phenomena. This specifically includes reactive mass transfer, which leads to a mass transfer enhancement and, thus, also increases the accompanying

volume effect. Such investigations are needed to improve the understanding of local processes in chemical engineering devices, such as bubble column reactors.

Acknowledgement

The second author gratefully acknowledges financial support by the Deutsche Forschungsgemeinschaft (DFG) within the Priority Program SPP 1740 “Reactive Bubbly Flows” under the grant BO1879/13-1.

Appendix A. Mathematical tools for volume averaging

This appendix provides the averaging tools which are used in Section 2.2.1 to derive the basic equations underlying the numerical method of this paper. With the definitions (24) and (25) of the volume and phase average, respectively, the following rules for interchanging differentiation and averaging can be derived for scalar quantities ϕ and vector valued Φ , cf. [13],

$$\langle \partial_t \phi \rangle_{V^k} = \partial_t \langle \phi \rangle_{V^k} - \langle \phi \mathbf{v}^\Sigma \cdot \mathbf{n}^k \rangle_{V^k}, \quad (\text{A.1})$$

$$\langle \nabla \phi \rangle_{V^k} = \nabla \langle \phi \rangle_{V^k} + \langle \phi \mathbf{n}^k \rangle_{V^k}, \quad (\text{A.2})$$

$$\langle \nabla \cdot \Phi \rangle_{V^k} = \nabla \cdot \langle \Phi \rangle_{V^k} + \langle \Phi \cdot \mathbf{n}^k \rangle_{V^k}, \quad (\text{A.3})$$

with the outer normal \mathbf{n}^k of phase Ω^k . Furthermore, note that for a solenoidal vector field \mathbf{v} , we can compute the divergence of the phase average. To this end, we assume that the control volume is given by $V(\mathbf{x}) = \mathbf{x} + V_0$ for a fixed control volume V_0 . First, we compute

$$\begin{aligned} \frac{\partial \langle \mathbf{v}_i \rangle_{V^k}}{\partial \mathbf{x}_i} &= -\frac{1}{|V(\mathbf{x}) \cap \Omega^k|^2} \frac{\partial |V(\mathbf{x}) \cap \Omega^k|}{\partial \mathbf{x}_i} \int_{V(\mathbf{x}) \cap \Omega^k} \mathbf{v}_i(\mathbf{y}) d\mathbf{y} \\ &\quad + \frac{1}{|V(\mathbf{x}) \cap \Omega^k|} \frac{\partial}{\partial \mathbf{x}_i} \int_{V(\mathbf{x}) \cap \Omega^k} \mathbf{v}_i(\mathbf{y}) d\mathbf{y} \end{aligned} \quad (\text{A.4})$$

$$\begin{aligned} &= -\frac{1}{|V(\mathbf{x}) \cap \Omega^k|^2} \left(\frac{\partial}{\partial \mathbf{x}_i} \int_{V(\mathbf{x}) \cap \Omega^k} 1 d\mathbf{y} \right) \int_{V(\mathbf{x}) \cap \Omega^k} \mathbf{v}_i(\mathbf{y}) d\mathbf{y} \\ &\quad + \frac{1}{|V(\mathbf{x}) \cap \Omega^k|} \frac{\partial}{\partial \mathbf{x}_i} \int_{V(\mathbf{x}) \cap \Omega^k} \mathbf{v}_i(\mathbf{y}) d\mathbf{y}. \end{aligned} \quad (\text{A.5})$$

Then, with the Leibniz rule [13] we get

$$\begin{aligned} \frac{\partial \langle \mathbf{v}_i \rangle_{V^k}}{\partial \mathbf{x}_i} &= -\frac{1}{|V(\mathbf{x}) \cap \Omega^k|^2} \int_{\partial V \cap \Omega^k} \mathbf{n}_i dA \int_{V(\mathbf{x}) \cap \Omega^k} \mathbf{v}_i(\mathbf{y}) d\mathbf{y} \\ &\quad + \frac{1}{|V(\mathbf{x}) \cap \Omega^k|} \int_{\partial V \cap \Omega^k} \mathbf{v}_i \mathbf{n}_i dA. \end{aligned} \quad (\text{A.6})$$

Summing over all indices $i = 1, 2, 3$, we obtain for the divergence of the phase average

$$\text{div} \langle \mathbf{v} \rangle_{V^k} = -\frac{1}{|V(\mathbf{x}) \cap \Omega^k|} \int_{\partial V \cap \Omega^k} \mathbf{n} dA \cdot \langle \mathbf{v} \rangle_{V^k} + \frac{1}{|V(\mathbf{x}) \cap \Omega^k|} \int_{\partial V \cap \Omega^k} \mathbf{v} \cdot \mathbf{n} dA \quad (\text{A.7})$$

$$\begin{aligned} &= -\frac{1}{|V(\mathbf{x}) \cap \Omega^k|} \int_{\partial V \cap \Omega^k} \mathbf{n} dA \cdot \langle \mathbf{v} \rangle_{V^k} + \frac{1}{|V(\mathbf{x}) \cap \Omega^k|} \int_{\Sigma \cap V(\mathbf{x})} \mathbf{n}^k dA \cdot \langle \mathbf{v} \rangle_{V^k} \\ &\quad + \frac{1}{|V(\mathbf{x}) \cap \Omega^k|} \int_{\partial V \cap \Omega^k} \mathbf{v} \cdot \mathbf{n} dA - \frac{1}{|V(\mathbf{x}) \cap \Omega^k|} \int_{\Sigma \cap V(\mathbf{x})} \mathbf{v} \cdot \mathbf{n}^k dA \end{aligned} \quad (\text{A.8})$$

$$= \frac{1}{|V(\mathbf{x}) \cap \Omega^k|} \int_{\Sigma \cap V(\mathbf{x})} (\langle \mathbf{v} \rangle_{V^k} - \mathbf{v}) \cdot \mathbf{n}^k dA + \langle \text{div} \mathbf{v} \rangle_{V^k}. \quad (\text{A.9})$$

In the last step, we used the fact that $\int_G \mathbf{n} dA = 0$ for all sufficiently regular volumes G .

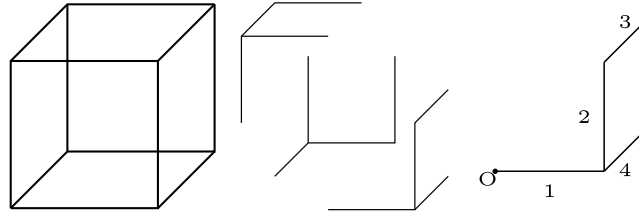


Fig. B.13. Decomposition of a hexahedral cell graph.

If the resolution of the interface is high enough in numerical computations, i.e. for small control volumes V , the contribution of the integral over the interface part $\Sigma \cap V(x)$ nearly vanishes in the last equation. In this case, the divergence of the phase averaged velocity $\langle \mathbf{v} \rangle_{V^k}$ can be approximated via

$$\text{div} \langle \mathbf{v} \rangle_{V^k} \approx \langle \text{div} \mathbf{v} \rangle_{V^k}. \quad (\text{A.10})$$

Since all relevant hydrodynamic scales must be resolved in a Direct Numerical Simulation, we can safely employ (A.10) in our numerical modeling.

Appendix B. Calculating the centroid of a PLIC element

Computing the centroid of the PLIC surface in interface cells is an essential part of the unsplit mass transfer algorithm in Section 3. Here, we provide a simple method to determine the centroid of such a PLIC element in cuboid cells which does not rely on triangulation. Such a cuboid cell is described by three cell lengths $\mathbf{d} = (d_1, d_2, d_3)^T$ and the location of the PLIC surface is given by the linear equation

$$\mathbf{n} \cdot \mathbf{x} = \ell, \quad (\text{B.1})$$

where \mathbf{n} is the normal of the PLIC element. In the current representation, \mathbf{n}, ℓ and the origin O of the coordinate system are such that O resides at a corner of the cuboid and the entries of \mathbf{n} are non-negative. Then the graph which defines the cell can be decomposed into three rotationally similar branches as shown in Fig. B.13.

With the setup above, computing the centroid of the PLIC surface consists of the steps:

1. compute the intersections of the PLIC element P with the edges of the cell
2. use the (ordered) set of intersection points \mathbf{p}_i to calculate the centroid \mathbf{x}_{PLIC}

The decomposition presented in Fig. B.13 allows to retrieve directly the (positively oriented) ordered set of points \mathbf{p}_i . This is achieved by calculating the intersections on each branch as shown in the figure. Then, there are only three possible configurations on each branch, which can be calculated analytically:

1. P intersects edge 1 alone
2. P intersects edge 4 and edge 2 (in this order)
3. P intersects edge 4 and edge 3 (in this order)

After the \mathbf{p}_i have been computed on a specific branch, a circular shift is performed on \mathbf{n} and \mathbf{d} , i.e., $\mathbf{n} = (n_1, n_2, n_3)^T \rightarrow \mathbf{n}^* = (n_3, n_1, n_2)^T$. This allows to repeat the calculation of the intersection points on a single branch, but then the entries of the intersection points must be “back shifted” since the entries of \mathbf{n} and \mathbf{d} have been permuted. Computing all intersection points then becomes:

1. choose one branch of the cuboid
2. repeat three times:
 - (a) compute the intersections on the current branch
 - (b) back-shift of the computed intersection points, yields \mathbf{p}_i
 - (c) save the current \mathbf{p}_i
 - (d) circular shift of \mathbf{n} and \mathbf{d}

With the intersections computed above, the centroid of P can be easily computed by employing the divergence theorem:

$$\mathbf{x}_{\text{PLIC}} = \frac{1}{3|A|} \sum_{i=1}^N \frac{1}{2} (\mathbf{p}_i + \mathbf{p}_{i+1}) |\mathbf{p}_i - \mathbf{p}_{i+1}| \left(\mathbf{p}_i \cdot \frac{\mathbf{p}_i - \mathbf{p}_{i+1}}{\|\mathbf{p}_i - \mathbf{p}_{i+1}\|} \times \mathbf{n} \right), \quad (\text{B.2})$$

where N is the number of intersections and $\mathbf{p}_{N+1} := \mathbf{p}_1$. The area $|A|$ of the PLIC polygon can be computed in the same manner as

$$|A| = \frac{1}{2} \sum_{i=1}^N |\mathbf{p}_i - \mathbf{p}_{i+1}| \left(\mathbf{p}_i \cdot \frac{\mathbf{p}_i - \mathbf{p}_{i+1}}{\|\mathbf{p}_i - \mathbf{p}_{i+1}\|} \times \mathbf{n} \right). \quad (\text{B.3})$$

References

- [1] C. Albert, H. Marschall, D. Bothe, Direct numerical simulation of interfacial mass transfer into falling films, *Int. J. Heat Mass Transf.* (2014) 343–357.
- [2] D. Bothe, On the multiphysics of mass transfer across fluid interfaces, in: F.-P. Schindler, M. Kraume (Eds.), 7th International Workshop – IBW7 on Transport Phenomena with Moving Boundaries and More, Fortschritt.-Ber. VDI Reihe 3, Nr. 947, VDI-Verlag, Düsseldorf, 2015, pp. 1–23.
- [3] D. Bothe, W. Dreyer, Continuum thermodynamics of chemically reacting fluid mixtures, *Acta Mech.* 226 (2015) 1757–1805.
- [4] D. Bothe, S. Fleckenstein, A Volume-of-Fluid-based method for mass transfer processes at fluid particles, *Chem. Eng. Sci.* 101 (2013) 283–302.
- [5] J. Brackbill, D. Kothe, C. Zemach, A continuum method for modeling surface tension, *J. Comput. Phys.* 100 (2) (1992) 335–354.
- [6] J. Crank, *The Mathematics of Diffusion*, Oxford University Press, 1975.
- [7] S. Fleckenstein, Modeling and direct numerical simulation of mass transfer from rising gas bubbles, Ph.D. thesis, Technische Universität Darmstadt, 2013.
- [8] C. Focke, D. Bothe, Computational analysis of binary collisions of shear-thinning droplets, *J. Non-Newton. Fluid Mech.* 166 (14–15) (2011) 799–810.
- [9] C. Gotaas, P. Havelka, H.A. Jakobsen, H.F. Svendsen, M. Hase, N. Roth, B. Weigand, Effect of viscosity on droplet–droplet collision outcome: experimental study and numerical comparison, *Phys. Fluids* 19 (2007) 102106.
- [10] J. Hadamard, Mouvement permanent lent d’une sphère liquide et visqueuse dans un liquide visqueux, *C. R. Acad. Sci. Paris* 152 (1911) 1735–1738.
- [11] S. Hardt, F. Wondra, Evaporation model for interfacial flows based on a continuum-field representation of the source terms, *J. Comput. Phys.* 227 (11) (2008) 5871–5895.
- [12] K. Hayashi, A. Tomiyama, Interface tracking simulation of mass transfer from a dissolving bubble, *J. Comput. Multiph. Flows* 3 (4) (2011) 247–262.
- [13] H.A. Jakobsen, *Chemical Reactor Modeling*, Springer-Verlag, Berlin, 2008.
- [14] G. Juncu, Unsteady-state mass transfer from a binary gas bubble with changing volume, *Int. J. Heat Mass Transf.* 54 (1–3) (2011) 669–677.
- [15] D. Juric, G. Tryggvason, Computations of boiling flows, *Int. J. Multiph. Flow* 24 (3) (1998) 387–410.
- [16] M. Koebe, D. Bothe, H.-J. Warnecke, Direct numerical simulation of air bubbles in water/glycerol mixtures: shapes and velocity fields, in: *Proceedings of 4th ASME-JSME Joint Fluids Engineering Conference*, 2003. Paper no. 45154.
- [17] C. Kunkelmann, P. Stephan, CFD simulation of boiling flows using the Volume-of-Fluid method within OpenFOAM, *Numer. Heat Transf., Part A, Appl.* 56 (8) (2009) 631–646.
- [18] C. Ma, D. Bothe, Numerical modeling of thermocapillary two-phase flows with evaporation using a two-scalar approach for heat transfer, *J. Comput. Phys.* 233 (2013) 552–573.
- [19] C. Ma, *Mathematische Modellierung und Direkte Numerische Simulation oberflächenspannungsgetriebener Zweiphasenströmungen mit und ohne Verdunstung*, Ph.D. thesis, Technische Universität Darmstadt, 2013.
- [20] H. Marschall, S. Boden, C. Lehrenfeld, C.J. Falconi D., U. Hampel, A. Reusken, M. Wörner, D. Bothe, Validation of interface capturing and tracking techniques with different surface tension treatments against a Taylor bubble benchmark problem, *Comput. Fluids* (2014) 336–352.
- [21] H. Oelrich, H. Schmidt-Traub, H. Brauer, Theoretische Berechnung des Stofftransports in der Umgebung einer Einzelblase, *Chem. Eng. Sci.* 28 (1973) 711–721.
- [22] F. Pigeonneau, Mass transfer of a rising bubble in molten glass with instantaneous oxidation–reduction reaction, *Chem. Eng. Sci.* 64 (13) (2009) 3120–3129.
- [23] F. Pigeonneau, D. Martin, O. Mario, Shrinkage of an oxygen bubble rising in a molten glass, *Chem. Eng. Sci.* 65 (10) (2010) 3158–3168.
- [24] W.J. Rider, D.B. Kothe, Reconstructing volume tracking, *J. Comput. Phys.* 141 (1997) 112–152.
- [25] M. Rieber, *Numerische Modellierung der Dynamik freier Grenzflächen in Zweiphasenströmungen*, Ph.D. thesis, Universität Stuttgart, 2004.
- [26] M. Rieber, A. Frohn, A numerical study on the mechanism of splashing, *Int. J. Heat Fluid Flow* 20 (5) (1999) 455–461.
- [27] W. Rybczynski, Über die fortschreitende Bewegung einer flüssigen Kugel in einem zähen Medium, *Bull. Inst. Acad. Sci. Cracovie, A* (1911) 40–46.
- [28] W. Sabisch, *Dreidimensionale numerische Simulation der Dynamik von aufsteigenden Einzelblasen und Blasenschwärmen mit einer Volume-of-Fluid-Methode*, Ph.D. thesis, Universität Karlsruhe, 2000.
- [29] Y. Sato, B. Ničeno, A sharp-interface phase change model for a mass-conservative interface tracking method, *J. Comput. Phys.* 249 (2013) 127–161.
- [30] J. Schlottke, *Direkte Numerische Simulation von Mehrphasenströmungen mit Phasenübergang*, Ph.D. thesis, Universität Stuttgart, 2010.
- [31] J. Schlottke, B. Weigand, Direct numerical simulation of evaporating droplets, *J. Comput. Phys.* 227 (10) (2008) 5215–5237.
- [32] J. Slattery, *Advanced Transport Phenomena*, Cambridge University Press, New York, 1999.
- [33] J. Slattery, J.L. Sagis, E.-S. Oh, *Interfacial Transport Phenomena*, Springer, Berlin, 2007.
- [34] F. Takemura, A. Yabe, Rising speed and dissolution rate of a carbon dioxide bubble in slightly contaminated water, *J. Fluid Mech.* 378 (1) (1999) 319–334.
- [35] F. Takemura, Y. Matsumoto, Dissolution rate of spherical carbon dioxide bubbles in strong alkaline solutions, *Chem. Eng. Sci.* 55 (18) (2000) 3907–3917.
- [36] F. Takemura, A. Yabe, Gas dissolution process of spherical rising gas bubbles, *Chem. Eng. Sci.* 53 (15) (1998) 2691–2699.
- [37] R. Taylor, R. Krishna, *Multicomponent Mass Transfer*, Wiley, 1993.
- [38] A. Tomiyama, S. Abe, K. Hayashi, S. Hosokawa, Dissolution of carbon dioxide bubbles in clean and contaminated systems, in: 5th European–Japanese Two-Phase Flow Group Meeting, 2009 (20–25 September).
- [39] B. van Leer, Towards the ultimate conservative difference scheme. IV. A new approach to numerical convection, *J. Comput. Phys.* 23 (3) (1977) 276–299.
- [40] S.W. Welch, J. Wilson, A volume of fluid based method for fluid flows with phase change, *J. Comput. Phys.* 160 (2) (2000) 662–682.
- [41] S. Whitaker, *The Method of Volume Averaging, Theory and Applications of Transport in Porous Media*, vol. 13, Springer, 1999.
- [42] M. Wörner, W. Sabisch, G. Grötzbach, D. Cacuci, Volume-averaged conservation equations for volume-of-fluid interface tracking, in: *Fourth International Conference on Multiphase Flow, ICMF-2001*, New Orleans, Louisiana, U.S.A., May 27–June 1, 2001, 2001.